

**PUBLICATIONS OF  
THE UNIVERSITY OF EASTERN FINLAND**

*Dissertations in Forestry and  
Natural Sciences*



UNIVERSITY OF  
EASTERN FINLAND

**WENJUAN CUI**

**FABRICATION OF DURABLE ICEPHOBIC SURFACES: EFFECTS  
OF SURFACE PROPERTIES AND LUBRICANT-INFUSED LAYER**



FABRICATION OF DURABLE ICEPHOBIC  
SURFACES: EFFECTS OF SURFACE  
PROPERTIES AND LUBRICANT-INFUSED  
LAYER



*Wenjuan Cui*

FABRICATION OF DURABLE ICEPHOBIC  
SURFACES: EFFECTS OF SURFACE  
PROPERTIES AND LUBRICANT-INFUSED  
LAYER

Publications of the University of Eastern Finland  
Dissertations in Forestry and Natural Sciences  
No 355

University of Eastern Finland  
Joensuu  
2019

Academic dissertation

To be presented by permission of the Faculty of Science and Forestry for  
public examination in the Auditorium F100 in the Futura Building at the  
University of Eastern Finland, Joensuu, on November, 26, 2019, at 12  
o'clock noon

Grano Oy

Jyväskylä, 2019

Editor: Nina Hakulinen

Distribution: University of Eastern Finland / Sales of publications

[www.uef.fi/kirjasto](http://www.uef.fi/kirjasto)

ISBN: 978-952-61-3238-9 (print)

ISSNL: 1798-5668

ISSN: 1798-5668

ISBN: 978-952-61-3239-6 (pdf)

ISSNL: 1798-5668

ISSN: 1798-5676

Author's address: Wenjuan Cui  
University of Eastern Finland  
Department of Chemistry  
P.O. Box 111  
80101 JOENSUU, FINLAND  
email: wenjuan.cui@uef.fi

Supervisors: Professor Emeritus Tapani Pakkanen, Ph.D.  
University of Eastern Finland  
Department of Chemistry  
P.O. Box 111  
80101 JOENSUU, FINLAND  
email: tapani.pakkanen@uef.fi

Professor Mika Suvanto, Ph.D.  
University of Eastern Finland  
Department of Chemistry  
P.O. Box 111  
80101 JOENSUU, FINLAND  
email: mika.suvanto@uef.fi

Reviewers: Professor Jouni Pursiainen, Ph.D  
University of Oulu  
Department of Chemistry  
P.O. Box 3000  
90014 OULU, FINLAND  
email: jouni.pursiainen@oulu.fi

Associate Professor Matti Putkonen, Ph.D  
University of Helsinki  
Department of Chemistry  
P.O. Box 55  
00014 HELSINKI, FINLAND  
email: matti.putkonen@helsinki.fi

Opponent: Associate Professor Rafael J. Taboryski, Ph.D  
Technical University of Denmark  
Department of Micro- and Nanotechnology  
2800 KONGENS LYNGBY, DENMARK  
email: rata@dtu.dk





Cui, Wenjuan

Fabrication of durable icephobic surfaces: effects of surface properties and lubricant-infused layer

Joensuu: University of Eastern Finland, 2019

Publications of the University of Eastern Finland

Dissertations in Forestry and Natural Sciences 2019; 355

## ABSTRACT

The icephobic performance of bioinspired superhydrophobic surfaces (SHSs), including lotus and petal surfaces, has received significant attention in recent years. Herein, the icephobic performance of rod-coated, structured polypropylene (PP), and smooth polymer surfaces with tunable wettability are clarified with several observational techniques. An assessment of the effects of wettability and surface energy on ice adhesion ( $\tau_{ice}$ ) reveal that petal and lotus surfaces lose their superhydrophobicity under sub-zero conditions. It is also shown that the  $\tau_{ice}$  values of rough surfaces increase with hydrophobicity and smooth hydrophobic surfaces with low surface energy have better icephobic performance than rough surfaces.

The limitations of SHSs in anti-icing applications have focused attention on bioinspired lubricant-infused slippery surfaces (LISSs). However, little work has been done to determine the effects of LISS material parameters on ice repellency. To analyze these effects, we spin-coated lubricant-elastomer layers (LELs) of varying thicknesses onto smooth and structured PP surfaces using a one-step approach. It was found that smooth LISSs coated with a thick LEL have ultra-low contact angle hysteresis (CAH) and  $\tau_{ice}$  compared to SHSs and smooth surfaces. LISSs also have superior dynamic mobility, stability, transparency, anti-dusting, and self-repairing. Increasing the thickness of the LEL coating on the smooth PP reduces the  $\tau_{ice}$ .

To clarify the effects of surface energy, oil, and nanoparticle content on icephobic performance, durable one-step silicone-oil-infused slippery coatings were prepared and used to produce a grid map of wetting behavior for tuning the wettability, morphology, and slippery properties. An analytic relationship between oil and nanoparticle content and  $\tau_{ice}$  was also developed. Results revealed that LISSs with slight hydrophobicity have slippery properties and an order magnitude lower  $\tau_{ice}$  than the  $\tau_{ice}$  found in SHSs. The 20-wt% silicone-oil-infused slippery coatings with small amounts of nanoparticles are potential in icephobic applications.

**Universal Decimal Classification:** 532.6, 539.61, 544.72

**Library of Congress Subject Headings:** Surfaces (Physics); Surface chemistry; Hydrophobic surfaces; Ice prevention and control; Adhesion; Polymers; Elastomers; Polypropylene; Surface energy; Coatings; Silicones; Lubrication and lubricants; Nanoparticles

## ACKNOWLEDGEMENTS

This study was carried out at the Department of Chemistry, the University of Eastern Finland from 2016-2019. Financial supports from the Business Finland innovation funding agency (Speed and Tyres), the European Union/European Regional Development Fund, and the Faculty of Science and Forestry (SCITECO grant) of the University of Eastern Finland are gratefully acknowledged.

I would like to express my deepest gratitude to Professor Emeritus Tapani Pakkanen for allowing me to do my Master's research and continue my Doctoral studies in the field of surface chemistry. Your invaluable support, encouragement, experience, and guidance motivated me to develop a scientific understanding in this field. I also owe profound gratitude to Professor Mika Suvanto for your perpetual support, advice, and encouragement throughout the research process.

I would especially like to thank Professor Emeritus Tuula Pakkanen, who gave support and advice on the study of lubricant analysis.

I would further like to thank Dr. Yu Jiang, Dr. Anna Kirveslahti, Dr. Kati Mielonen, and MSc. Kai Ikonen for your cooperation. In addition, my appreciation goes to all the staff members of the Department of Chemistry, University of Eastern Finland, especially to Docent Nina Hakulinen, Dr. Sari Suvanto, Dr. Leila Alvila, Dr. Lena Ammosova, Dr. Ville Nissinen, MSc. Hanna Paananen, Ms. Päivi Inkinen, Mr. Martti Lappalainen, Mr. Urpo Ratinen, Ms. Taina Nivajärvi, and Ms. Mari Heiskanen for your practical advice. Special thanks go to my officemates, Chian Ye and Aderemi.

My warmest gratitude also goes to Linlin, Jinnan, Leo, Meidi, Chenyang, and all of my friends for your company during my stay in Joensuu.

I am grateful to my parents, younger brother, parents-in-law, and other family members for your encouragement, support, and care. Finally, I wish to give my special thanks to my dear husband Xinxin and our upcoming little baby for your constant love and support.

Joensuu, 2019

*Wenjuan Cui*

## LIST OF ABBREVIATIONS

AAO	anodic aluminum oxide
ACA	advancing contact angle
BMIm	1-butyl-3-methylimidazolium bis(trifluoromethylsulfonyl)imide
CAH	contact angle hysteresis
CC	closed-cell
CNT	classical nucleation theory
DC	dry-coated
DMPA	dimethylolpropionic acid
DSC	differential scanning calorimetry
IPA	isopropyl alcohol
LECC	lubricant-elastomer infused closed-cell
LEL	lubricant-elastomer layer
LEOC	lubricant-elastomer infused open-cell
LESPP	lubricant-elastomer infused smooth polypropylene
LIC	lubricant-infused coated
LICLE	lubricant-infused cross-linked elastomer
LINMC	lubricant-infused nanoparticle modified coating
LISP	lubricant-infused smooth polymer
LISS	lubricant-infused slippery surface
MNPP	polypropylene with micro-nano-structures
MPP	polypropylene with micro-pillars
MPR	melt-processible rubber
NMC	nanoparticle modified coating
NPP	polypropylene with nano-pillars
OC	open-cell
PAA	poly(acrylic acid)
PC	polycarbonate resin
PDMS	polydimethylsiloxane
PE	polyethylene
PES	polyester
PES-0	blank polyester
PET	polyethylene terephthalate
PFD	perfluorodecalin
PFPP	perfluoroperhydrophenanthrene
PMMA	poly(methylmethacrylate)
PP	polypropylene
PS	polystyrene
PU	polyurethane
PVC	polyvinyl chloride
PVDF	polyvinylidene fluoride

RCA	receding contact angle
RIIDC	repeated icing/ice-detachment cycles
SANC	self-assembled nanoparticle coating
SEM	scanning electron microscope
SHS	superhydrophobic surface
SiO <sub>2</sub> NPs	silica nanoparticles
SLIPS	slippery liquid-infused porous surface
SMPR	smooth melt-processible rubber
SPC	smooth polycarbonate resin
SPDMS	smooth polydimethylsiloxane
SPE	smooth polyethylene
SPMMA	smooth poly(methylmethacrylate)
SPP	smooth polypropylene
SST	shear stability test
STHV	smooth fluorothermoplastic
TCL	triple-phase contact line
THV	fluorothermoplastic
TST	thermal stability test
WCA	water contact angle

## LIST OF PARAMETERS

$\tau_{ice}$	ice adhesion shear strength
$P_w$	wetting pressure
$P_{EWH}$	effective water hammer pressure
$P_c$	capillary pressure
$We$	Weber number
$Re$	Reynolds number
$Oh$	Ohnesorge number
$\rho$	droplet density
$V_0$	impact velocity
$D$	initial droplet diameter
$\mu$	droplet viscosity
$\sigma$	surface tension
$J$	ice nucleation rate
$\Delta G$	free Gibbs energy
$K$	kinetic prefactor
$k_B$	Boltzmann constant
$r_c$	critical radius
$\gamma^{IW}$	ice-water interfacial energy
$\Delta G_{f,v}$	difference in volumetric free energy of bulk ice vs bulk liquid
$\Delta H$	volumetric fusion heat of ice melting

$T_m$	melting temperature
$W_{adh}$	work of adhesion of liquid droplet on a solid surface
$\gamma_{LV}$	liquid-vapor surface tension of a liquid droplet
$F$	ice adhesion strength
$F_{adh}$	ice adhesive strength
$F_{coh}$	ice cohesive strength
$\phi$	air-water contact area fraction
$\gamma_{SV}$	solid-vapor interface tension/surface energy of solid
$\gamma_{SL}$	solid-liquid interface tension
$\theta^*$	water contact angle on a rough surface
$R$	surface roughness factor
$\phi_s$	solid contact area fraction at a liquid-solid interface
$\gamma^C$	critical surface free energy
$b$	slope of the Zisman plot
$\gamma_{SV}^d$	dispersive component for the surface energy of a solid
$\gamma_{LV}^d$	dispersive component for the surface tension of a liquid droplet
$\gamma_{SV}^P$	polar component for the surface energy of a solid
$\gamma_{LV}^P$	polar component for the surface tension of a liquid droplet
$S_{ow(a)}$	oil-water spreading coefficient in the presence of air
$\gamma_{wa}$	surface tension of water droplet
$\gamma_{wo}$	water-oil interfacial energy
$\gamma_{oa}$	surface tension of oil/lubricant
$\gamma_{so}$	solid-oil interface tension
$\gamma_{sw}$	solid-water interface tension
$\theta$	water contact angle
$\theta_{oa}$	contact angle of oil on a smooth solid surface
$\theta_{wa}$	contact angle of water on a smooth solid surface
$\theta_{adv}$	advancing contact angle
$\theta_{rec}$	receding contact angle
$t_d$	freezing delay time
$E$	intrinsic surface energy
$a_c$	diameter at the top of a micro-pit
$b_c$	diameter at the bottom of a micro-pit
$c_c$	distance between the tops of two adjacent micro-pits
$d_c$	distance between the bottom necks of two adjacent micro-pits
$H_c$	height of the micro-pit
$a_o$	diameter at the top of a micro-pillar
$b_o$	diameter at the bottom of a micro-pillar
$c_o$	distance between the upper necks of two adjacent micro-pillars
$d_o$	distance between the bottoms of two adjacent micro-pillars
$H_o$	height of a micro-pillar
$S_t$	sliding time



## LIST OF ORIGINAL PUBLICATIONS

This thesis is based on data presented in the following articles, referred to by roman numerals I-III, respectively:

- I Cui W, Jiang Y, Mielonen K, Pakkanen T.A. (2019). The verification of icephobic performance on biomimetic superhydrophobic surfaces and the effect of wettability and surface energy. *Applied Surface Science*, 466: 503-514.
- II Cui W, Pakkanen T.A. (2019). Fabrication of transparent icephobic surfaces with self-reparability: effect of structuring and thickness of the lubricant-elastomer layer. *Applied Surface Science*, In press.
- III Cui W, Pakkanen T.A. (2019). Icephobic performance of one-step silicone-oil-infused slippery coatings: effects of surface energy, oil and nanoparticle contents. *Journal of Colloid and Interface Science*, 588: 251-258.

## OTHER RELATED PUBLICATIONS BY THE AUTHOR DURING THE STUDY:

- Kirveslahti A, Mielonen K, Ikonen K, Cui W, Suvanto M, Pakkanen T.A. (2016). Underwater sliding properties: effect of slider shape and surface wettability. *Surface Review and Letters*, 23: 1650042.

## AUTHOR'S CONTRIBUTION

The main ideas for the topics in **Publications I-III** were developed from discussions between the author and several co-authors.

- I. The author planned and developed the observational techniques for assessing icephobic performance. The author performed all the experimental work and wrote the manuscript, with the exception of the description of the preparation of structured polypropylene surfaces.
- II. The author performed all the experimental work and wrote the manuscript.
- III. The author performed all the experimental work and wrote the manuscript.



# CONTENTS

<b>1</b>	<b>INTRODUCTION.....</b>	<b>15</b>
1.1	Fundamentals of icephobic materials .....	16
1.1.1	Droplet impact dynamics .....	17
1.1.2	Supercooling and ice nucleation.....	18
1.1.3	Ice adhesion .....	20
1.2	Surface properties .....	21
1.2.1	Surface structure .....	22
1.2.2	Wettability .....	23
1.2.3	Surface energy .....	26
1.3	Typical icephobic materials .....	27
1.3.1	Superhydrophobic surfaces.....	28
1.3.2	Lubricant-infused slippery surfaces.....	29
1.3.2.1.	Overview.....	29
1.3.2.2.	Stability.....	30
1.4	Aims of the study .....	33
<b>2</b>	<b>EXPERIMENTAL .....</b>	<b>34</b>
2.1	Coated surfaces.....	34
2.2	Polymer surfaces.....	35
2.2.1	Dry polymer surfaces.....	35
2.2.2	Slippery lubricant-infused polymer surfaces.....	36
2.3	Characterization.....	36
<b>3</b>	<b>RESULTS AND DISCUSSION.....</b>	<b>37</b>
3.1	Dry surfaces.....	37
3.1.1	Surface properties .....	37
3.1.2	Icephobic performance .....	39
3.2	Slippery lubricant-elastomer infused polymer surfaces.....	42
3.2.1	Surface properties .....	42
3.2.2	Icephobic performance .....	44
3.3	Slippery lubricant-infused coated surfaces.....	47
3.3.1	Surface properties .....	47
3.3.2	Icephobic performance .....	49
<b>4</b>	<b>CONCLUSIONS.....</b>	<b>51</b>
<b>5</b>	<b>BIBLIOGRAPHY.....</b>	<b>52</b>



# 1 INTRODUCTION

Biomimetics has an important reference value for scientists to study smart materials and face environmental challenges. Research on bioinspired surface materials with special functions has received extensive attention in some fields. These fields include chemistry, materials science, physics, engineering, and biomedicine.[1]

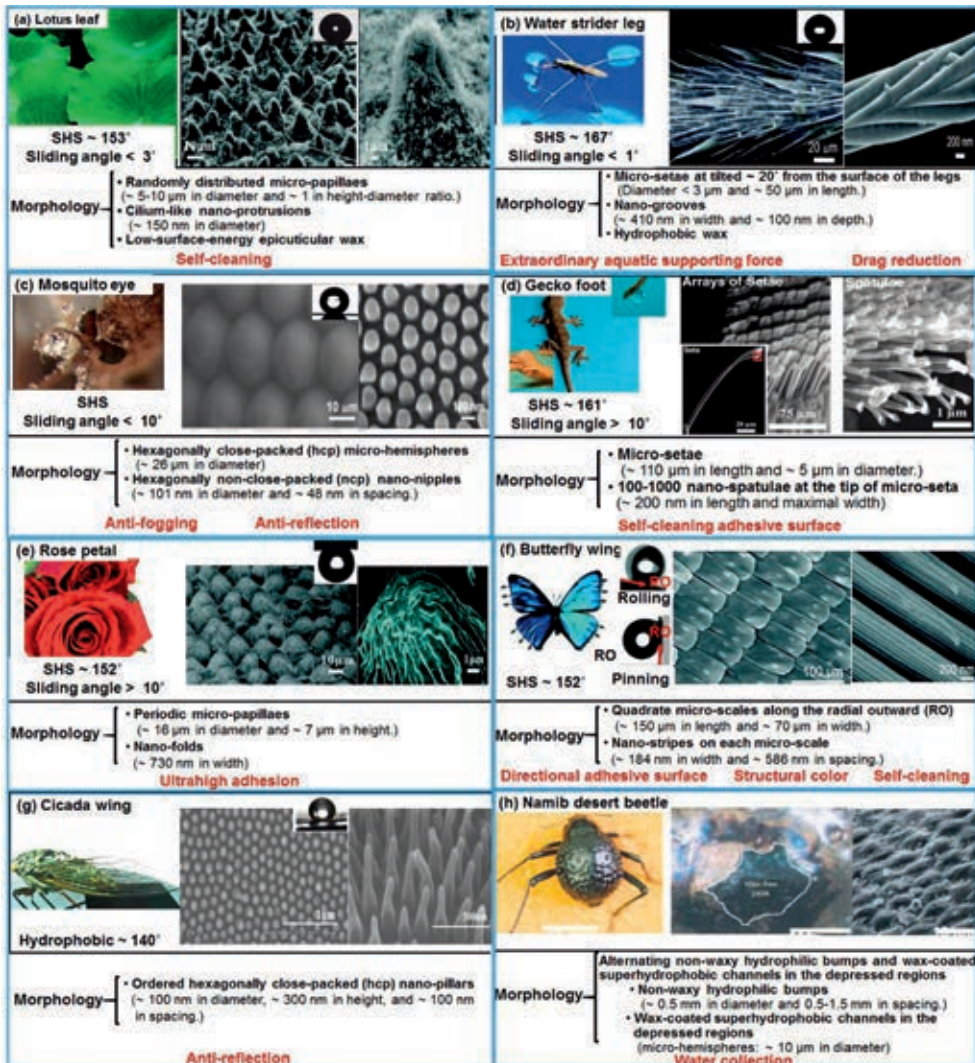


Figure 1. Wettability, morphology, and functions of structures found on various organisms. (a) Lotus leaf reproduced from ref. [2,3]. (b) Water strider leg reproduced from ref. [1,4-7]. (c) Mosquito eye reproduced from ref. [8-10]. (d) Gecko foot reproduced from ref. [11,12]. (e) Rose petal reproduced from ref. [13]. (f) Butterfly wing reproduced from ref. [14-16]. (g) Cicada wing reproduced from ref. [17-19]. (h) Namib desert beetle reproduced from ref. [20].

Plants and animal structural surfaces with special functions are common in nature. Examples these include superhydrophobic surfaces (SHSs) with low adhesion, which are found on self-cleaning lotus leaves,[2] water-walking water spiders,[4] and mosquitos with anti-fog and anti-reflective eyes.[8] High-adhesion SHSs, another common feature, are found in rose petals[13] and self-cleaning gecko feet.[11] Other examples include butterfly wings with directional adhesion and structural coloring,[14] anti-reflective cicada wings,[17] and water-collecting Namib desert beetle backs.[20] The wettabilities, morphologies, and functionalities of these organismal structures are illustrated in Figure 1. The surface chemistries and morphologies of such structures can serve as an inspiration for the development of new synthetic surfaces.

The agglomeration of ice, frost, wet-snow, and supercooled water droplets (0-500  $\mu\text{m}$ ) under cold conditions can negatively affect exposed outdoor infrastructures such as air-sea-land transportation facilities and energy systems.[21,22] Strategies to mitigate the formation and accumulation of ice can be divided into active de-icing and passive icephobic approaches.

Examples of the active approach include electrothermal (heating), chemical (salts), and mechanical removal (scraping, vibration, or twisting) methods. However, the active approaches can be environmentally unfriendly, energy- and time-consuming, and expensive.[23,24] Since the 1950s, much research has focused on the development of preventive, economic, effective, and low-pollution-icephobic materials.[25–27] Notably, the number of passive icephobic strategies developed has increased significantly from 2004.[28]

## 1.1 FUNDAMENTALS OF ICEPHOBIC MATERIALS

The research on icephobic and anti-icing materials has rapidly increased in recent years. (Figure 2) An icephobic surface is defined as one in which the ice adhesion shear strength ( $\tau_{\text{ice}}$ ) less than 100 kPa,[29,30] and a  $\tau_{\text{ice}}$  of below  $\sim 55$  kPa allows for the self-removal of formed ice by a strong breeze.[31]

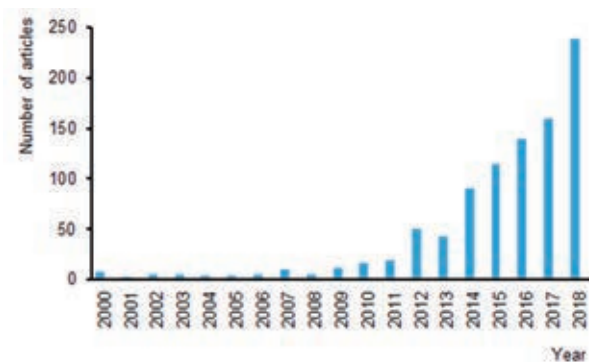


Figure 2. Number of articles published per year on icephobic or anti-icing topics. (Obtained from Web of Science).

An optimal icephobic material will: i) inhibit the sticking and minimize the contact time of impinging supercooled water/ice (dynamic property); ii) delay ice nucleation (static property); and iii) have a low adhesion shear strength for ice that forms on its surfaces.[23,27,32]

In designing icephobic materials, it is particularly important to understand the complex nature of icing. Icephobic strategies are generally aimed at ice reduction either before or after icing. Before icing, the icephobic strategies involve either dynamic droplet impact or static ice nucleation.

### 1.1.1 Droplet impact dynamics

Droplet impact dynamics can be divided into three stages. The first stage is spreading, during which a droplet spreads radially outward until it achieves its maximum diameter. The second stage is a retraction, and the third stage is the equilibrium or rebound phase, in which the diameter of the droplet remains constant. If the energy of the droplet is sufficiently large, it can rebound.[33–35] Figures 3a-b demonstrate the effects of impact velocity and surface properties on impact behavior.[36]

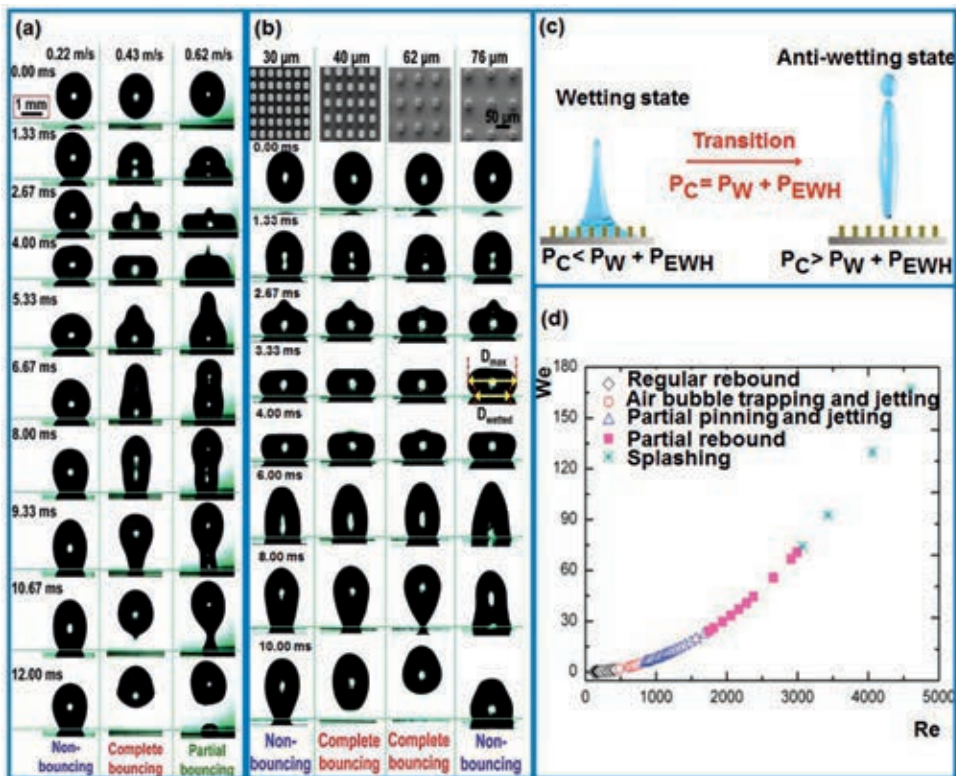


Figure 3. (a) Effect of impact velocity on impact behavior. (b) Effect of surface structure on impact behavior. (Adapted from ref. [36]) (c) Schematics of wetting and anti-wetting states.[37] (d) Impact behavior of droplet at different Reynolds and Weber numbers.[38]

The impact behavior of a droplet is affected by two downward pressures and an upward pressure. The downward pressures are the wetting pressure ( $P_w$ ) and the effective water hammer pressure ( $P_{EWH}$ ), both of which cause the droplet to penetrate the micro-nano-structures of the surfaces. Although the droplet impact will, in general, be asymmetrical,  $P_{EWH}$  arises only from the velocity component perpendicular to the surface. The upward pressure is the capillary pressure ( $P_c$ ), which acts to prevent the droplet from penetrating the surface structures. When  $P_c$  is less than the sum of the two downward pressures, the impacting droplet will stick to the surface; otherwise, the impacting droplet remains on the surface in an anti-wetting state. (Figure 3c)[37,39]

Several dimensionless parameters are used to characterize droplet impact dynamics, including the Weber ( $We$ ), Reynolds ( $Re$ ), Ohnesorge ( $Oh$ ) numbers, and the factor  $K$ . [36,40]

$$Re = \frac{\rho V_0 D}{\mu} = \frac{\text{inertial forces}}{\text{viscous forces}} \quad (1)$$

$$We = \frac{\rho V_0^2}{\sigma} = \frac{\text{inertial forces}}{\text{surface tension}} \quad (2)$$

$$Oh = \frac{\mu}{\sqrt{\rho \sigma D}} = \frac{\sqrt{We}}{Re} = \frac{\text{viscous forces}}{\sqrt{\text{inertial forces} * \text{surface tension}}} \quad (3)$$

$$K = Oh * Re^{1.25} \quad (4)$$

where,  $\rho$ ,  $V_0$ ,  $D$ ,  $\mu$ , and  $\sigma$  are the droplet density, impact velocity, initial droplet diameter, droplet viscosity, and surface tension, respectively. The effects of  $Re$  and  $We$  on the impact behavior are shown in Figure 3d. [38] When the value of  $K$  is greater than 57.7, splashing occurs. [40]

One very effective approach to preventing icing is to ensure that impinging droplets fall before freezing, which can be achieved if the contact time between the surface and the droplets during the slipping process is sufficiently reduced. [32,41]

### 1.1.2 Supercooling and ice nucleation

Under cold conditions, ice nucleation is inevitable. To achieve an anti-icing effect prior to freezing, it is essential to delay ice nucleation or reduce the freezing temperature, which can be achieved by changing the surface morphology and/or chemistry. [32]

The formation of ice nuclei requires a thermodynamic energy barrier, [42] and the formation and subsequent growth of critical ice nuclei take a certain amount of time. [23] Therefore, before the water nucleates bulk water will remain in the liquid metastable state below the equilibrium melting temperature (0 °C) in a condition referred to as a supercooled state. [43]

According to classical nucleation theory (CNT), its initial minimum size of a critical ice nucleus appears at air-water and/or external solid-water interfaces.

(Figure 4a) Formation at an air-water interface corresponds to homogeneous nucleation, which acts on the bulk volumetric liquid phase by evaporative cooling. Homogeneous nucleation generally occurs at a temperature below  $-40\text{ }^{\circ}\text{C}$ . Formation at a solid-water interface corresponds to heterogeneous nucleation. In nature, liquids are often mixed with impurities (dust, bacteria, etc.) or in contact with container walls. In general, ice nucleation at above  $-40\text{ }^{\circ}\text{C}$  involves heterogeneous nucleation, which must overcome less free energy than homogeneous nucleation.[5,23] (Figure 4b)

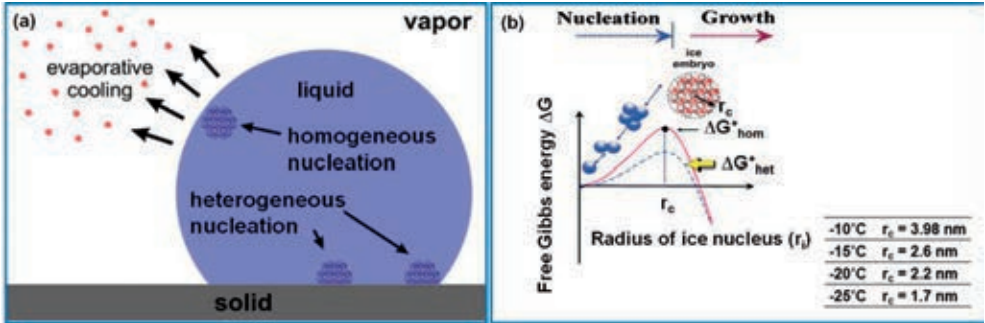


Figure 4. (a) Schematic of ice nucleation. (Adapted from ref. [28]) (b) Homogeneous and heterogeneous nucleation barriers based on classical nucleation theory. (Adapted from ref. [21,28,44,45])

Under the CNT, the ice nucleation rate of a supercooled water droplet on a surface ( $J$ ) is defined as:

$$J = K \exp\left(\frac{-\Delta G}{k_B T}\right) \quad (5)$$

where,  $\Delta G$  is the thermodynamic free Gibbs energy required to form a critical ice embryo and is also the maximum bulk free energy required during ice nucleation.  $K$  is a kinetic prefactor that expresses the diffusion of water molecules to form an ice embryo.  $k_B$  is the Boltzmann constant.  $T$  is the temperature.[46] The value of  $\Delta G$  is dependent on the actual contact area.[47]

The formation of ice involves the formation and subsequent growth of a critical ice embryo. The ice nucleus remains thermodynamically stable until reaching a critical radius ( $r_c$ ), after which it grows spontaneously.[48] The value of  $r_c$  is calculated as follows:

$$r_c = \frac{2\gamma_{IW}}{\Delta G_{f,v}} \quad (6)$$


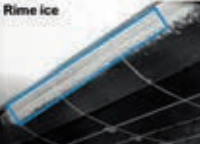
$$\gamma_{IW} = 28.0 + 0.25T \quad (7)$$

$$\Delta G_{f,v} = \frac{\Delta H(T_m - T)}{T_m} \quad (8)$$

where,  $\gamma_{IW}$  is the ice-water interfacial energy in units of  $\text{mJ}/\text{m}^2$ .  $\Delta G_{i,v}$  is the difference in volumetric free energy between the bulk ice and the bulk liquid.  $\Delta H$  is the volumetric fusion heat of ice melting, which is  $350 \text{ MJ}/\text{m}^3$  at  $-10 \text{ }^\circ\text{C}$ .  $T_m$  is the melting temperature ( $273 \text{ K}$ ).[\[21,28,49\]](#) When the roughness of a low-surface-energy solid surface is lower than  $r_c$ , ice nucleation will be delayed, resulting in a condition similar to homogeneous nucleation.[\[41\]](#)

Under humid conditions, chilled surfaces will rapidly condense microdroplets ( $\geq 10 \text{ }\mu\text{m}$ ) and frost, resulting in the nucleation of ice.[\[23,27\]](#) The formation mechanisms, features, and densities of the two main physical icing types (glaze and rime) are listed in [Table 1](#).[\[50\]](#)

Table 1. Formation mechanisms, features, and densities of different ice types.[\[50–52\]](#)

Type of ice	Mechanism of ice formation	Feature of ice	Ice density
	Supercooled freezing rain, drizzle, and wet snow with a diameter ranging from $70 \text{ }\mu\text{m}$ to a few millimeters completely wet a solid surface to form glaze ice.	Transparent high density hard difficult to remove	$\sim 0.9 \text{ g}/\text{cm}^3$
	In high-humidity cold conditions, supercooled water vapor with a diameter ranging from $5\text{-}70 \text{ }\mu\text{m}$ freezes quickly on a solid surface.	Soft rime low density white brittle	$0.2\text{-}0.6 \text{ g}/\text{cm}^3$
		Hard rime Opaque low-medium strength	$0.7\text{-}0.9 \text{ g}/\text{cm}^3$

### 1.1.3 Ice adhesion

The ice adhesion shear strength ( $\tau_{ice}$ ), which is the maximum force required to remove ice per unit area of cross-section,[\[53\]](#) is an important parameter for characterizing ice repellency following water nucleation.[\[27\]](#) The work of adhesion of a liquid droplet on a solid surface ( $W_{adh}$ ) can be calculated using the Young-Dupré equation based on the redefinition of Gao and McCarthy:[\[54–56\]](#)

$$W_{adh} = \gamma_{LV}(1 + \cos \theta_R) \tag{9}$$

where,  $\gamma_{LV}$  is the liquid-vapor surface tension of the liquid droplet and  $\theta_R$  is the receding contact angle.

At a molecular level, the  $\tau_{ice}$  on a solid surface originates from van der Waals forces, electrostatic interaction, hydrogen bonding, or covalent chemical bonding. However, only solid surfaces with hydroxyl groups can induce hydrogen bonding. Only surfaces with specific chemical and crystal arrangements can produce covalent chemical bonding at a distance range of  $0.1\text{-}0.2 \text{ nm}$ . Thus, for most solid surfaces the van der Waals force and electrostatic interaction are the mechanisms producing  $\tau_{ice}$ . The electrostatic interaction is caused by interattraction between the charge on the



ice surface and induced charge on the solid surface. Mechanical interlocking creates the van der Waals force, which can be affected by viscoelastic properties.[32,57–60]

When the ice layer and the solid surface textures have mechanical interlocking, the ice adhesion strength ( $F$ ) is expressed with the following equation. (Figure 5a)

$$F = F_{adh} + \phi(F_{coh} + F_{adh}) \quad (10)$$

where,  $F_{adh}$  is the adhesive strength.  $\phi$  is the air-water contact area fraction.  $F_{coh}$  is the cohesive strength.[61] The value of the cohesive force is about 1600 kPa and is much greater than the adhesive force.[23] Therefore, this explains the rough surface with mechanical interlocking effect has a large ice adhesion.

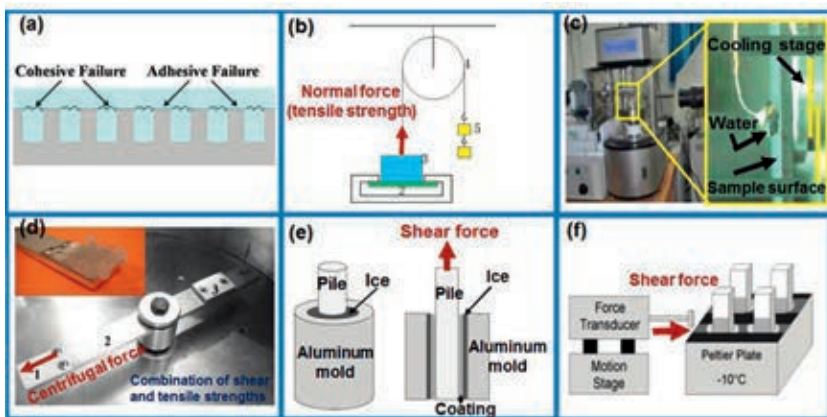


Figure 5. (a) Model of cohesive and adhesive failure on a rough surface with mechanical interlocking effect.[61] (b) Ice adhesion obtained through normal force.[62] (c) Ice adhesion measured through sessile microdroplet adhesion with a surface tension tester.[63] (d) Ice adhesion measured through centrifugal force.[64] (e) Ice adhesion measured through 0° cone test method.[65] (f) Ice adhesion measured by horizontal force gauge.[55]

The measured value of ice adhesion depends on the measurement method used and the type of icing. To date no uniform standard has been developed to measure ice adhesion;[32] in general, five approaches are used, as shown in Figure 5b-f.

## 1.2 SURFACE PROPERTIES

There have been a number of recent studies on the relationship between ice adhesion and dry material parameters. Meuler et al. reported that, when the receding contact angle is less than 120° on a smooth surface,  $\tau_{ice}$  and the parameter  $(1+\cos\theta_{rec})$  are linear.[55] Under certain conditions, linear correlations between  $\tau_{ice}$  and surface energy, water contact angle, and contact angle hysteresis have also been reported.[58,66–68] The effects of lubricant-infused slippery surface (LISS) parameters on icephobic applications have also been explored. Vogel et al. showed that closed-cell (CC) structures are superior to open-cell (OC) structures in the

immobilization of lubricant.[69] Liu et al. demonstrated the effects of surface chemistry, length scale, and surface morphology on freezing delay time, ice adhesion, and lubricant retention.[70] These studies show how icephobic materials can be achieved through the control of surface properties such as surface structure and energy and wettability.

### 1.2.1 Surface structure

Surface modification techniques typically involve physical and chemical methods. The most common physical methods include photolithography, femtosecond laser ablation, plasma etching, spin coating, spray coating, electrospinning, template method, ion-assisted deposition, and phase separation. The most common chemical methods include sol-gel method, electrochemical deposition, atomic layer deposition, layer-by-layer deposition, and hydrothermal synthesis.[71,72] (Figures 6-7)

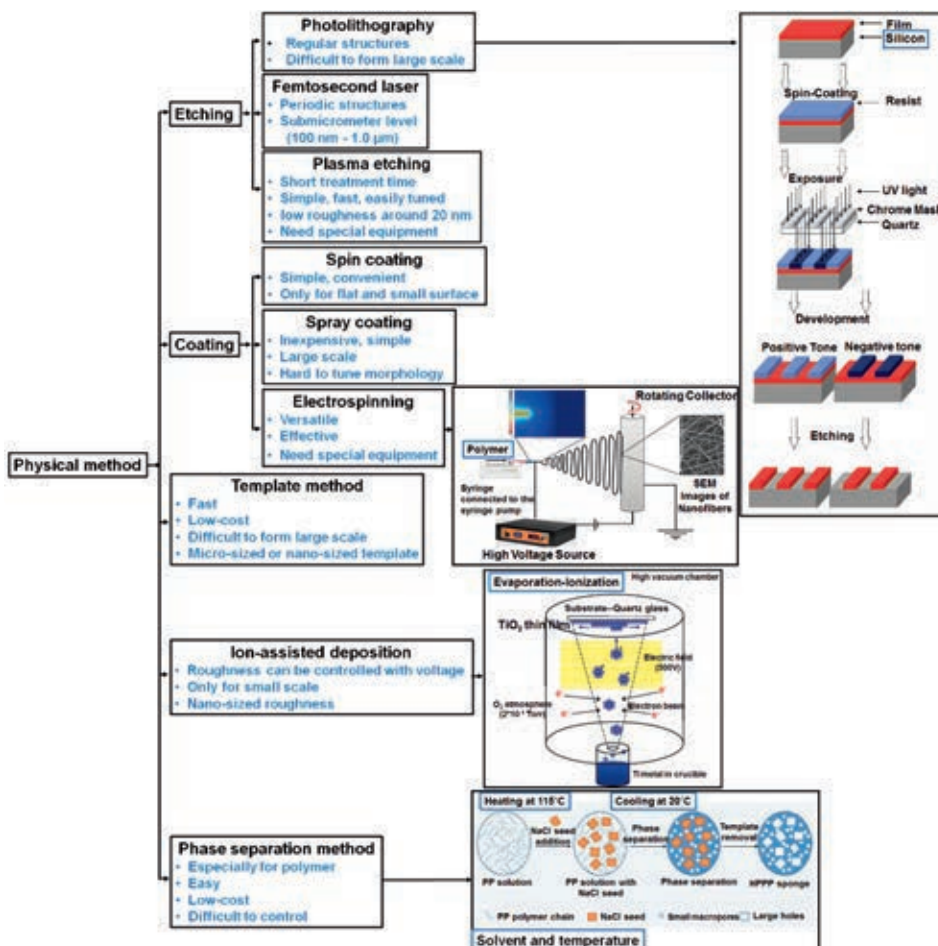


Figure 6. Characteristics of physical methods.[71,72] The schematics of the photolithography, electrospinning, ion-assisted deposition, and phase separation reproduced from ref.[73–76].

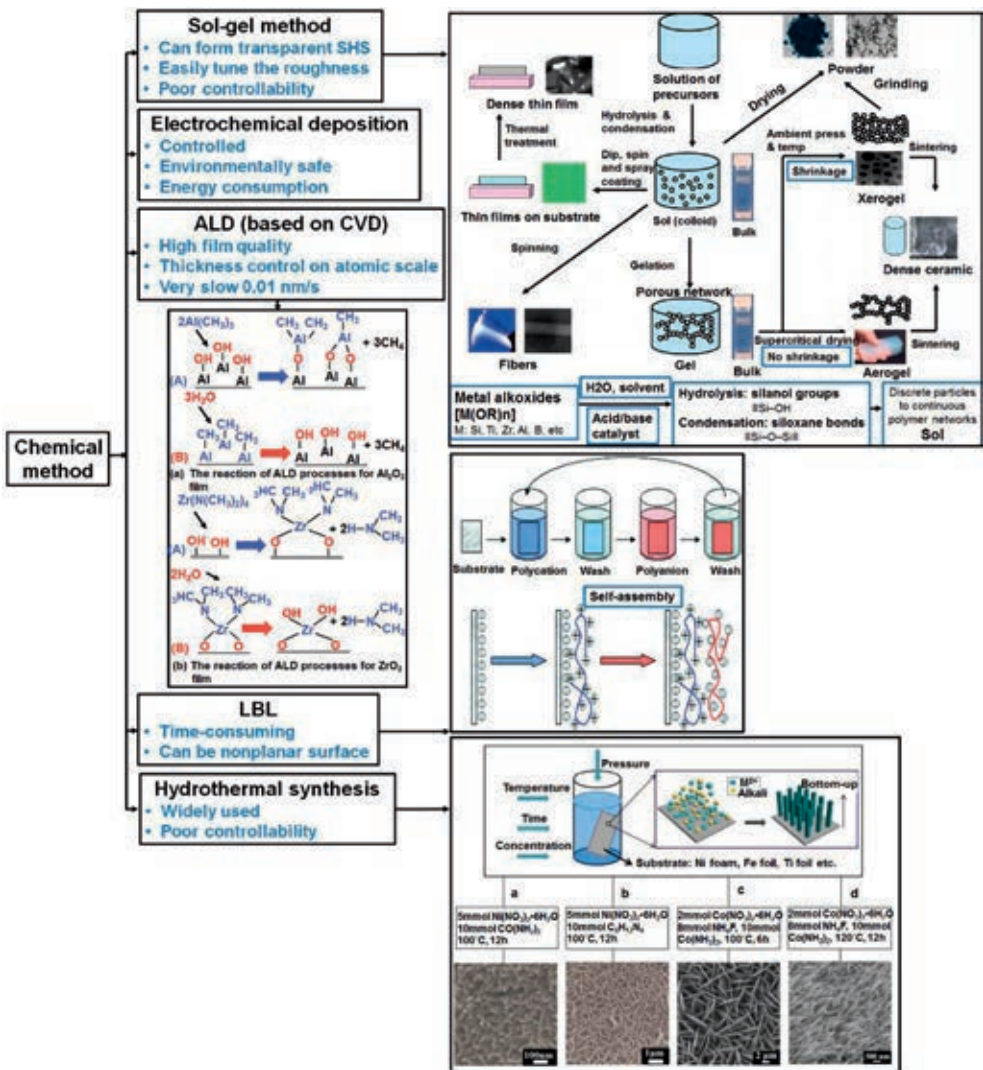


Figure 7. Characteristics of chemical methods.[71,72] The schematic of the sol-gel, atomic layer deposition, layer-by-layer deposition, and hydrothermal synthesis processes are reproduced from ref. [77–80].

## 1.2.2 Wettability

Surface wettability is a joint function of surface structure and chemical composition.[71,81] Wettability can be described in terms of the water contact angle (WCA). It is generally accepted that a solid surface will be hydrophilic when  $WCA < 90^\circ$ ; Conversely, the surface will be hydrophobic at  $WCA > 90^\circ$ . A solid surface with a  $WCA > 150^\circ$  is defined as a superhydrophobic surface (SHS). The contact angle hysteresis (CAH) is the difference between the advancing contact angle (ACA,  $\theta_{adv}$ ) and the receding contact angle (RCA,  $\theta_{rec}$ ).[82]

Hydrogen bonding between water molecules and a solid substrate are used to absorb water and produce an adhesive force. The strength of the adhesive force on a solid substrate depends on the magnitude of the hydrogen bonding. The cohesive force exists in the water. A hydrophobic surface will have a weak adhesive force and a strong cohesive force, while a hydrophilic surface will have a strong adhesive force and a weak cohesive force.[83,84] (Figure 8)

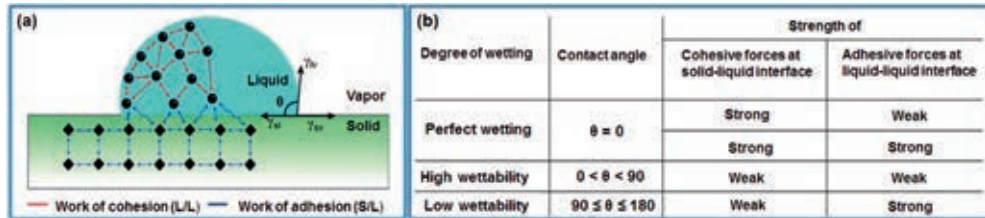


Figure 8. (a) Schematic of adhesive and cohesive forces at a liquid-solid interface.[85] (b) Relationship between wettability, water contact angle and interaction force.[86]

In the static state, wettability is determined by the interface balance of the three phases (solid, liquid, and vapor).[41] The WCA of a liquid droplet on an ideally smooth and chemically homogeneous surface is expressed with Young's equation, which was first proposed in 1805:[54]

$$\cos \theta = \frac{(\gamma_{SV} - \gamma_{SL})}{\gamma_{LV}} \quad (11)$$

where,  $\theta$  is the water contact angle.  $\gamma$  is the interface tension. Subscripts S, L, and V indicate solid, liquid, and vapor, respectively. (Figure 9a)

As Young's equation will be invalid for a liquid droplet on a rough surface, in 1936, Wenzel derived the following equation of wettability on a rough surface:[87] (Figure 9b)

$$\cos \theta^* = R \cos \theta \quad (12)$$

where,  $\theta^*$  is the WCA on a rough surface. R, the surface roughness factor, is the ratio of the actual area of the rough surface to its geometrically projected area. A water droplet in the Wenzel state will completely penetrate a textured structure, forming a homogeneous and continuous triple-phase contact line (TCL).[88]

However, the Wenzel model will not be effective for a solid texture with air pockets. To account for this, in 1944, Cassie and Baxter formulated the WCA on a heterogeneous rough solid surface:[89] (Figure 9c)

$$\cos \theta^* = \phi_S (\cos \theta + 1) - 1 \quad (13)$$

where,  $\theta^*$  is the WCA on a rough surface with a discontinuous TCL.  $\phi_S$  is the solid contact area fraction between the liquid droplet and the solid substrate.

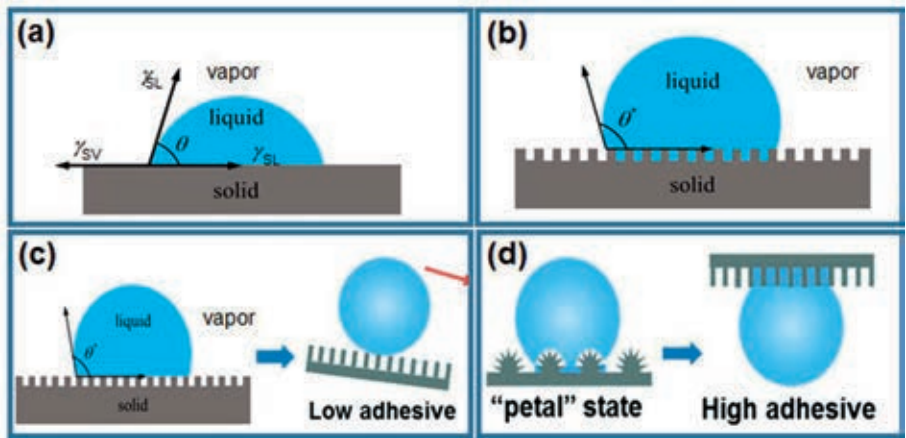


Figure 9. (a) Young's wetting mechanism.[88] (b) Wenzel wetting mechanism.[88] (c) Cassie-Baxter wetting mechanism.[88,90] (d) Wetting mechanism on petal surface.[90]

There are two representative SHS wetting modes: the lotus and petal states. When the CAH  $< 10^\circ$ , the SHS will be a lotus surface with a Cassie-Baxter state. A lotus surface will have low adhesion and self-cleaning property. (Figure 9c) The actual contact area between a droplet and lotus surface will generally be less than 10%.[91,92]

At CAH  $> 10^\circ$ , the SHS will be a petal surface with high adhesion. A water droplet on a petal surface will penetrate its micro-structures (Wenzel state) while leaving air cushions in the nanostructures (Cassie-Baxter state). As such, a petal surface will be in a Cassie-Wenzel intermediate state.[13] (Figure 9d)

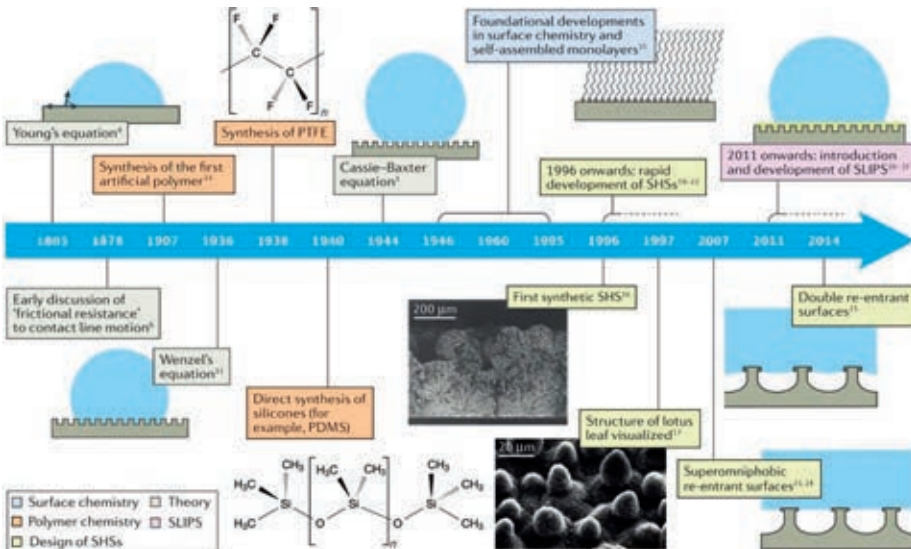


Figure 10. Timeline of major advances in the field of liquid repellency.[32]

### 1.2.3 Surface energy

Surface energy and surface tension are the energies used to define the unit surface area.[93] Surface tension is associated with the liquid surface, while the surface energy is used for solid surface. Surface energy is a characteristic parameter of the composition of the solid surface and is given in units of dyne/cm or mN/m.[94]

The surface energy of a solid affects its interaction with the surrounding media in terms of, e.g., adsorption, wetting, and adhesion.[95] The numerical value of surface energy is usually derived from measurements of the contact angle of a liquid on the solid's surface based on an application of Young's equation (Equation 11). In Young's equation,  $\gamma_{LV}$  and the contact angle  $\theta$  on an ideally flat surface can be obtained. As the solid-liquid interface tension  $\gamma_{SL}$  is not directly measurable,[95,96] the Zisman and Wu methods are used to calculate it and obtain the surface energy of the solid,  $\gamma_{SV}$ .

The Zisman method assumes that the surface energy of a solid will be equal to the maximum surface tension of a liquid for which the solid-liquid contact angle is  $0^\circ$ . The maximum surface tension of a liquid is defined as the critical surface free energy ( $\gamma_c$ ). The relationship between  $\theta$  and  $\gamma_{LV}$ , which is plotted in Figure 11, is derived as followed:

$$\cos \theta = 1 - b(\gamma_{LV} - \gamma_{SV}) \quad (14)$$

where,  $b$  is the slope of the Zisman plot. The Zisman method is only applicable to non-polar surfaces.[97]

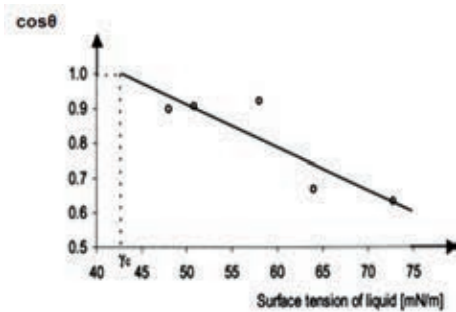


Figure 11. Zisman plot based on measured data.[98]

The Wu method applies the harmonic mean to describe the surface energy of a solid as the sum of the surface tensions of a dispersive ( $\gamma^d$ ) and polar components ( $\gamma^p$ ). Solid-liquid interfacial energy,  $\gamma_{SL}$ , can be expressed as follows:[99,100]

$$\gamma_{SL} = \gamma_{SV} + \gamma_{LV} - \frac{4\gamma_{SV}^d \gamma_{LV}^d}{\gamma_{SV}^d + \gamma_{LV}^d} - \frac{4\gamma_{SV}^p \gamma_{LV}^p}{\gamma_{SV}^p + \gamma_{LV}^p} \quad (15)$$

It had been shown that the surface energies of various hydrocarbon and fluorocarbon groups decreases in the following order:  $-\text{CH}_2 > -\text{CH}_3 > -\text{CF}_2 > -\text{CF}_2\text{H} > -\text{CF}_3$ . Research has indicated that the surface energy of a smooth surface aligned with hexagonal-closed-packed  $-\text{CF}_3$  groups can be as low as  $6.7 \text{ mJ/m}^2$ .<sup>[101]</sup>

### 1.3 TYPICAL ICEPHOBIC MATERIALS

Icephobic materials can have either a solid or liquid surfaces. Over the past few decades, research on icephobicity has discovered several classic icephobic materials.

Li et al. reported that the ice nucleation rate of a hydrophilic surface is about one order of magnitude lower than that of a hydrophobic surface.<sup>[102]</sup> Wang et al. demonstrated that a soft material polydimethylsiloxane (PDMS) elastomer (Sylgard 184) can be used for anti-icing applications because the difference in modulus between the ice and the soft material results in a strain mismatch when the ice is removed. Increasing the PDMS elastomer thickness reduces the ice adhesion.<sup>[103]</sup> (Figure 12a) Cui,<sup>[66]</sup> Bharathidasan,<sup>[104]</sup> and Susoff<sup>[65]</sup> et al. found that smooth surfaces with low surface energy and slight hydrophobicity can demonstrate low ice adhesion values. Good candidates for icephobic materials include low-surface-energy fluoropolymer, silicone polymer, and fluorosilicone copolymer coatings.<sup>[105]</sup>

Materials with lubricating layers have also been shown to be resistant to ice. Lubricating layers can be formed from the air (SHS), liquids (organic LISS or aqueous lubricating layer with hygroscopic polymers<sup>[106]</sup>), or other media. (Figure 12b) The other media include materials in which phase change releases heat,<sup>[107]</sup> antifreeze proteins,<sup>[108]</sup> or particles that display a photothermal effect under near-infrared irradiation.<sup>[109]</sup>

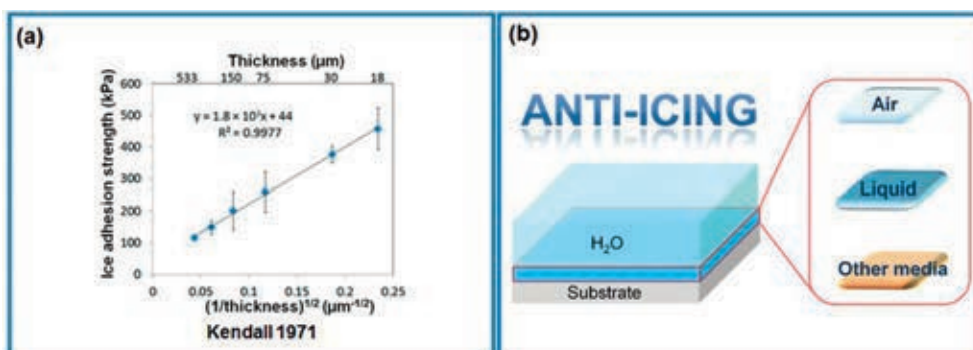


Figure 12. (a) Ice adhesion as a function of the square root of the inverse of the thickness  $(1/\text{thickness})^{1/2}$ .<sup>[103]</sup> (b) Anti-icing mechanisms of materials using air, liquid, or other media ad lubricating layers.<sup>[23]</sup>

A summary of the ice adhesion values of various materials is given in Figure 13. The most commonly studied of these materials in the context of icephobicity are SHSs and LISSs.

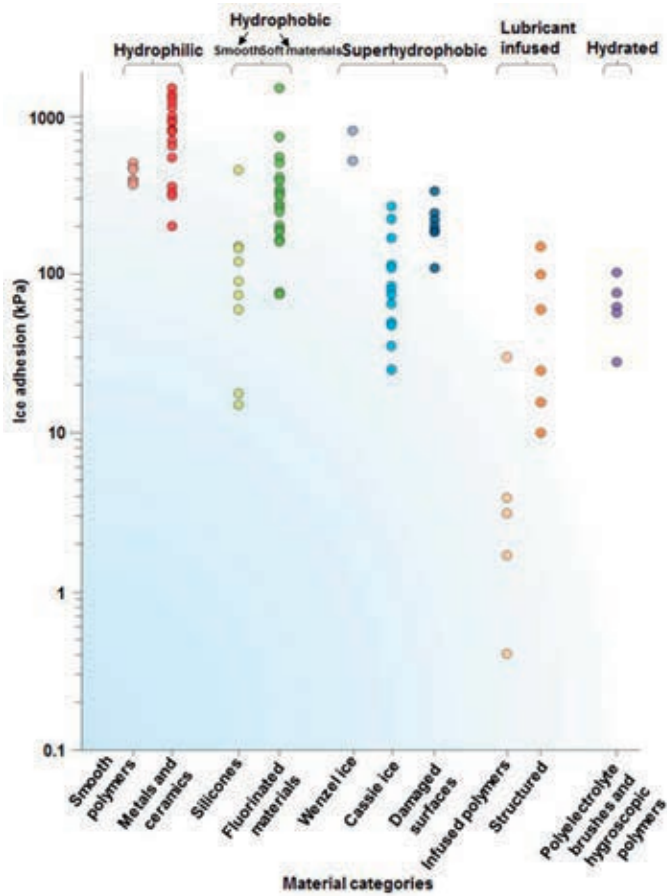


Figure 13. Summary of the ice adhesion values for various materials.[32]

### 1.3.1 Superhydrophobic surfaces

Owing to their extraordinary water repellency, SHSs are considered to have significant potential for use in icephobic applications. The main mechanism of the low ice adhesion on an SHS is the freezing of water in a Cassie-Baxter state, in which air pockets between the SHS and the ice reduce the actual contact area. In addition, the heterogeneous wetting state of the SHS reduces the amount of heat transfer, delaying the freezing of water on the cold surface.[23,92]

Kulinich et al. found that SHSs with low CAH exhibited ~ 4 - 5.7 times lower ice adhesion than smooth surfaces with similar surface chemistries.[64] He et al. demonstrated that, when the contact area fraction of solid on an SHS is less than 0.068, the SHS will maintain its superhydrophobicity at the dew point.[110] Guo et al. found that micro-nano-structured SHSs have the longer freezing delay times (~ 7000s) than either micro-structured, nano-structured, or smooth surfaces at -10 °C.[63]



Mishchenko et al. reported that at temperatures between -25 to -30 °C, impacting supercooled water would roll off a highly ordered SHS before freezing, resulting in an ice-free state.[111]

Not all SHSs, however, are icephobic. The limitations of SHS in their icephobic applications are that weak stabilities at high temperatures, pressures, humidities, and impact speeds, and weak mechanical resistances. [112–114]

Varanasi et al. showed that, in cold and humid environments, frost forms in the textures of an SHS, resulting in a transition from a Cassie-Baxter to a Wenzel state. The increased contact area significantly increases ice adhesion.[112] Kulinich et al. reported that, following several de-icing processes, the surface textures of an SHS are gradually destroyed, resulting in enhanced ice adhesion.[113] Surface structures damaged in this manner are difficult to repair, making SHSs generally useless in icephobic applications.

### **1.3.2 Lubricant-infused slippery surfaces**

#### **1.3.2.1. Overview**

In 2011, Aizenberg proposed a novel type of lubricant-infused slippery surface (LISS) inspired by *Nepenthes* plants, comprising a Teflon porous membrane and perfluorinated lubricants. Such surfaces exhibit an extraordinary slippery property and are omniphobic. In other words, they can repel various liquids, including water, hydrocarbons, crude oil, blood, and ice.[115]

LISSs have soft smooth surfaces with physical and chemical homogeneity. The lubricants completely wet solid surfaces through roughness, chemical affinity, or electromagnetic interaction. The LISSs exhibit extremely low CAHs and effective slippery properties even in high humidity environments.[53,69,115,116]

The commonly used solid materials and lubricants used to fabricate LISSs and the applications of the resulting surfaces are shown in [Figure 14](#). The fabrication of a conventional LISS is a two-step process involving the formation of a porous substrate followed by infusion of a lubricant layer. The lubricant locks in the porous textures via van der Waals and capillary forces.[115]

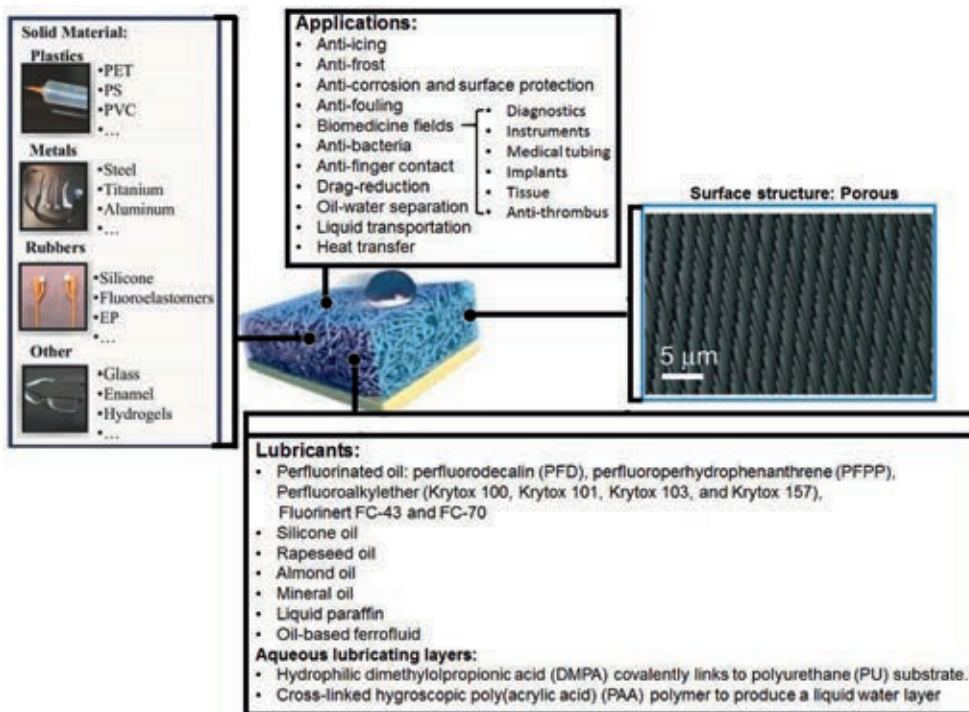


Figure 14. Commonly used solid materials, lubricants, surface structures, and applications of lubricant-infused slippery surfaces.[31,115,117–122]

In addition, the slippery property of a LISS will be activated by external stimuli such as temperature, magnetic or electric fields, mechanical stimuli, changes in pH, or light.[123] (Figure 15) For example, Wang et al. reported that a lubricant-infused porous graphene sponge covering a shape-memory polymer (*trans*-1,2-polyisoprene) had a slippery property in a compressed state. When the compressed structure rebounded under electrical stimulation, the surface lost its slippery property.

### 1.3.2.2. Stability

Because the lubricants in conventional LISSs are prone to depletion, migration, and evaporation, it is important to improve lubricant retention. The three criteria for maintaining thermodynamic stability are: i) the lubricant is non-volatile and unable to cloak the condensate liquid; ii) the lubricant and condensate liquid are immiscible; and iii) the lubricant wets the solid surface more easily than a condensate liquid.[114,115] Five common approaches to improving LISS stability are shown in Figure 15.

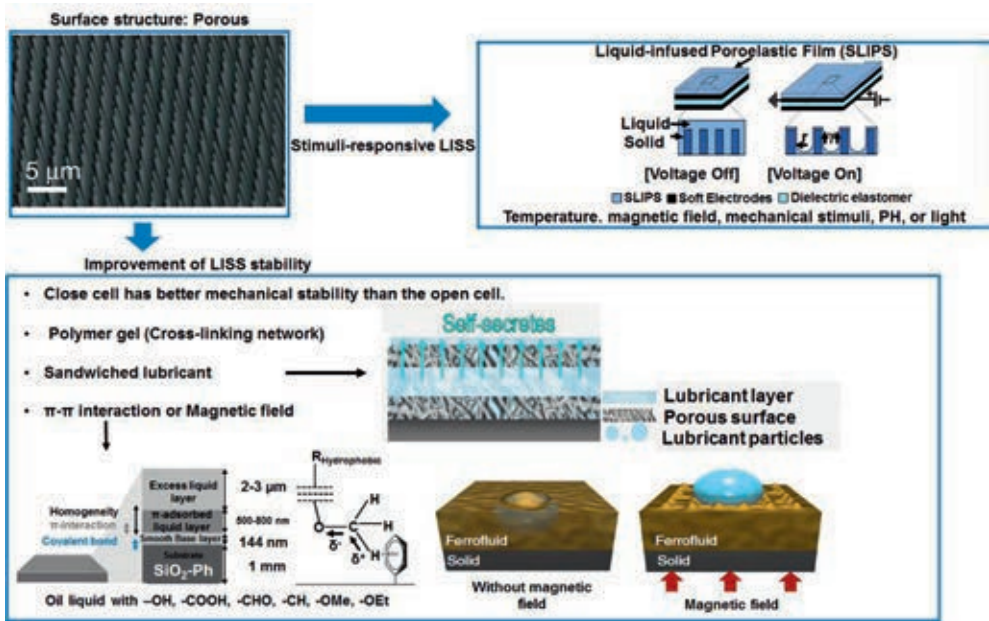


Figure 15. Stimuli-responsive lubricant-infused slippery surfaces (LISSs) and common approaches to improving LISS stability.[69,124–127]

The cloaking behavior of a water droplet is determined by its oil-water spreading coefficient in the presence of air ( $S_{ow(a)}$ ):[128]

$$S_{ow(a)} = \gamma_{wa} - \gamma_{wo} - \gamma_{oa} \quad (16)$$

where,  $\gamma$  is the interfacial tension. Subscripts o, w, and a correspond to oil/lubricant, water, and air, respectively. The condition  $S_{ow(a)} > 0$  corresponds to a lubricant that can cloak a water droplet and be easily lost through evaporation, while  $S_{ow(a)} < 0$  indicates that the water droplet is non-cloaking and the lubricant is non-volatile (Figure 16a-b). Sett et al. studied the cloaking behavior and solubility of several lubricants with different viscosities and working fluids. Their combined findings on cloaking behavior and solubility are shown in Figure 16c.

To understand the third criterion, that is, that the solid surface is more susceptible to wetting by the lubricant than by a test liquid, the interfacial energies of three configurations are considered. Under configuration W, the solid surface is completely wetted by the test liquid; Configurations 1 and 2 are that the solid surface is completely wetted by the lubricant with or without a layer of the test liquid, respectively. (Figure 16d) We can then represent the interfacial energies as:

$$\Delta E_1 = R(\gamma_{oa} \cos \theta_{oa} - \gamma_{wa} \cos \theta_{wa}) - \gamma_{ow} \quad (17)$$

$$\Delta E_2 = R(\gamma_{oa} \cos \theta_{oa} - \gamma_{wa} \cos \theta_{wa}) + \gamma_{wa} - \gamma_{oa} \quad (18)$$

where,  $E_W$ ,  $E_1$ , and  $E_2$  are the interfacial energies of Configurations W, 1, and 2, respectively.  $R$  is the surface roughness factor.  $\theta_{oa}$  and  $\theta_{wa}$  are the contact angles of oil and water on a smooth solid surface, respectively. When  $\Delta E_1 = E_W - E_1 > 0$  and  $\Delta E_2 = E_W - E_2 > 0$ , the third criterion is satisfied.[115]

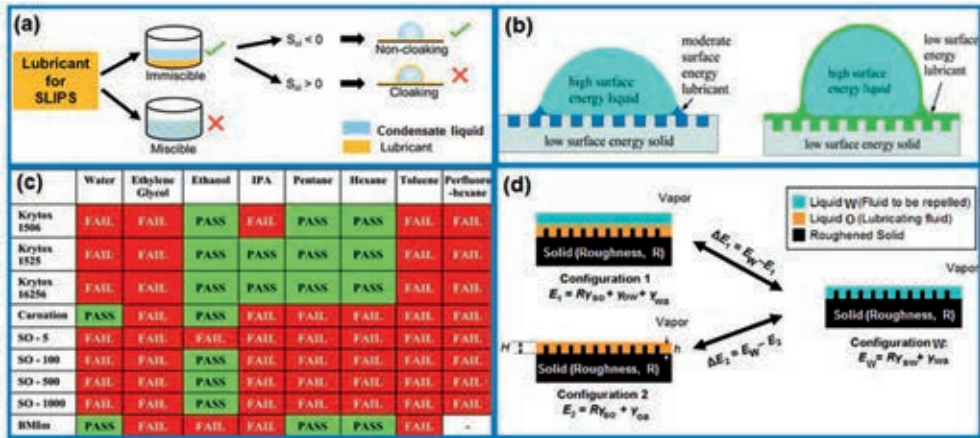


Figure 16. (a) Cloaking behavior and solubility between condensate liquid and lubricant on a LISS.[129] (b) Cloaking behavior of a water droplet on a textured surface infused with different surface-energy lubricants.[128] (c) Combined cloaking behavior and solubility results between various lubricants and working fluids: FAIL indicates miscible and cloaking lubricant-fluid pairs; PASS indicates immiscible and non-cloaking pairs; SO-5 indicates silicone oil with viscosity 5 cSt; Carnation oil indicates mineral oil; BMIIm indicates ionic liquid and 1-butyl-3-methylimidazolium bis(trifluoromethylsulfonyl)imide; IPA indicates isopropyl alcohol.[129] (d) Schematics of Configurations W, 1, and 2.[115]

## 1.4 AIMS OF THE STUDY

This study focused on dry rod-coated surfaces, structured polypropylene (PP) surfaces, smooth polymer surfaces, and lubricant-infused slippery surfaces (LISSs) to develop simple, low-cost, and durable icephobic materials. The following specific goals were addressed:

- Verification of icephobic performance on the smooth polymer, rough hydrophobic, petal, and lotus surfaces using several observational techniques;
- Assessment of the roles of wettability and surface energy on ice adhesion and heterogeneous ice nucleation;
- Development of icephobic applications through the fabrication of stable and durable LISSs with lubricant-elastomer layers using a facile one-step procedure;
- Assessment of the effects of underlying structures and lubricant-elastomer layer thickness on ice adhesion;
- Fabrication of eco-friendly and inexpensive LISSs via a fast, one-step coating approach;
- Assessment of the effects of oil and nanoparticle content and surface morphology and energy on the icephobic performance of LISSs.

## 2 EXPERIMENTAL

### 2.1 COATED SURFACES

Schematics of our processes for fabricating of dry-coated (DC) and slippery lubricant-infused coated (LIC) surfaces are shown in [Figure 17](#).



Figure 17. Processes for fabricating (a) dry-coated and (b) slippery lubricant-infused coated surfaces. The schemes are not drawn to scale.

To produce a self-assembled nanoparticle coating (SANC), a nanoparticle modified coating (NMC) solution was blended completely for 3 h at 1400 rpm. The NMC solution comprised a polyvinylidene fluoride (PVDF) binding agent, toluene solvent, and hydrophobic silica nanoparticles ( $\text{SiO}_2$  NPs, 14 nm). A simple and low-cost one-step rod coating method was used to coat the uniform NMC solution onto an aluminum (Al) substrate, and the coated surface was then cured at  $250^\circ\text{C}$  for two minutes to obtain the DC surface. A detailed description of the DC surface fabrication process is given in [Publication I](#). Each DC surface was designated as DC-w, where w is the weight percentage of  $\text{SiO}_2$  NPs.

To fabricate a slippery LIC surface, a silicone oil with a viscosity of 100 cP was added to an NMC solution with a volume ratio of PVDF, toluene, and silicone oil of 2/2/1 to produce a lubricant-infused nanoparticle modified coating (LINMC) solution. The well-blended LINMC solution was coated onto the Al substrate using a one-step rod coating method to produce a cured slippery LIC surface. A detailed description of LIC surface fabrication process is given in [Publication III](#). Each LIC surface was designated as LIC-x-y, where x and y are the weight percentages of silicone oil and  $\text{SiO}_2$  NPs, respectively.

## 2.2 POLYMER SURFACES

### 2.2.1 Dry polymer surfaces

Schematics of the structured polypropylene (PP) surface fabrication processes are shown in [Figure 18](#). A smooth PP (SPP) disc with a 25-mm diameter was fabricated directly using an injection molding method, while a PP with micro-pillars (MPP) was obtained by injection molding with a micro-structured Al mold. The micro-structured Al mold was made with a micro-working robot. A nano-structured PP (NPP) surface was fabricated by anodizing electropolished Al foil to produce a nanoporous anodic aluminum oxide (AAO) film, which was then injection-molded to produce an NPP surface. A micro-nano-porous Al mold was formed by anodizing an electropolished micro-structured Al foil, which was then injection-molded to produce a micro-nano-structured PP (MNPP) surface.

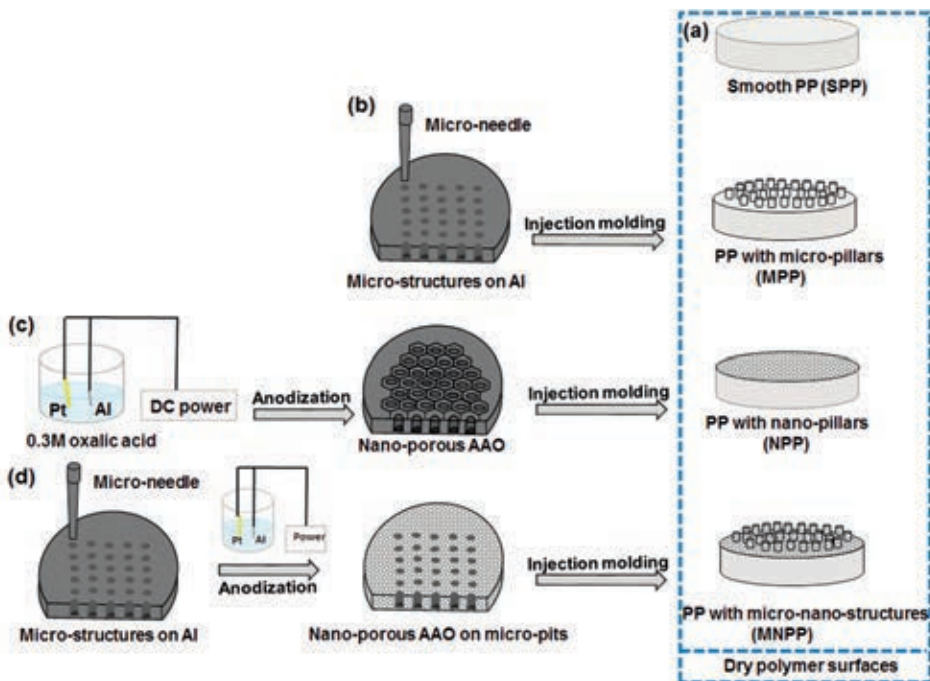


Figure 18. (a) Smooth polypropylene (SPP). (b) Fabrication of PP with micro-pillars (MPP). (c) Fabrication of nano-structured PP (NPP). (d) Fabrication of micro-nano-structured PP (MNPP). The schemes are not drawn to scale.

Several smooth dry polymer surfaces, including smooth fluorothermoplastic (STHV), polyethylene (SPE), melt-processible rubber (SMPR), polycarbonate resin (SPC), polyester (PES-0), and poly(methylmethacrylate) (SPMMA), were also fabricated. A detailed description of the fabrication of each structured PP and smooth polymer surfaces is given in [Publication 1](#).

## 2.2.2 Slippery lubricant-infused polymer surfaces

Schematics of the fabrication of several types of PP surface with a slippery lubricant-elastomer layer (LEL) are shown in [Figure 19](#). The dry SPP, closed-cell (CC), and open-cell (OC) surfaces were first formed. The CC and OC structures were high-aspect-ratio structured PP surfaces with micro-pits and micro-pillars, respectively. To increase the chemical affinity between the PP substrates and the LELs, the formed dry PP surfaces were modified using silanization. Homogeneous 40 wt-% PDMS, 60 wt-% silicone oil with 100-cP viscosity were then combined with PDMS curing agent (10:1 by weight) to form lubricant-infused cross-linked elastomer (LICLE) solutions. Finally, the LICLE solutions were coated on respective silanized PP substrates using a spin coating method and then cured to obtain PP surfaces with slippery LELs with thicknesses of 300  $\mu\text{m}$  and 600  $\mu\text{m}$ . The slippery lubricant-elastomer infused polymer surfaces were designated as LESPP, LECC, and LEOC. A detailed description of this process is given in [Publication II](#).

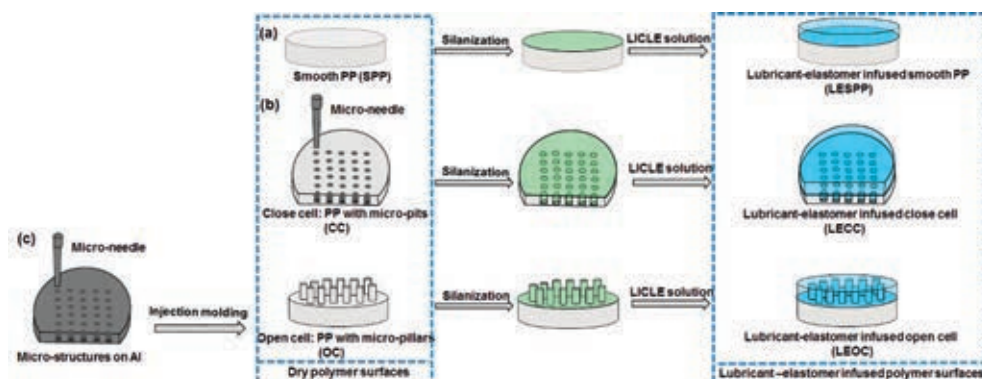


Figure 19. Fabrication of (a) LESPP, (b) LECC, and (c) LEOC. The schemes are not drawn to scale.

Six additional slippery lubricant-infused smooth polymer (LISP) surfaces were prepared via injection molding using 20 wt% silicone oil based on the polymers THV, PE, MPR, PC, PES, and PMMA. A detailed description of this process is given in [Publication III](#).

## 2.3 CHARACTERIZATION

The morphology and wettability of all specimens were characterized and the surface energies of the dry surfaces were also measured. The icephobic performance of each dry surface was assessed by applying an ice adhesion shear strength test ([Figure 20a](#)), differential scanning calorimetry (DSC), and a delayed ice nucleation test ([Figure 20b](#)), as described in [Publication I](#).

The icephobic performance of each slippery lubricant-infused polymer surface was quantified by applying an ice adhesion shear strength test. The optical



transmittance of each PP surface with a slippery LEL was determined using a UV-Vis-NIR spectrometer. The dynamic mobility, stability, and self-repairing characteristics of each PP surface with a slippery LEL were also examined, as described in [Publication II](#).

The icephobic performance of each LIC surface was measured using an ice adhesion shear strength test and the DSC method. The lubricant retention capability of each LIC surface was determined by applying a lubricant shear stability test, as described in [Publication III](#).

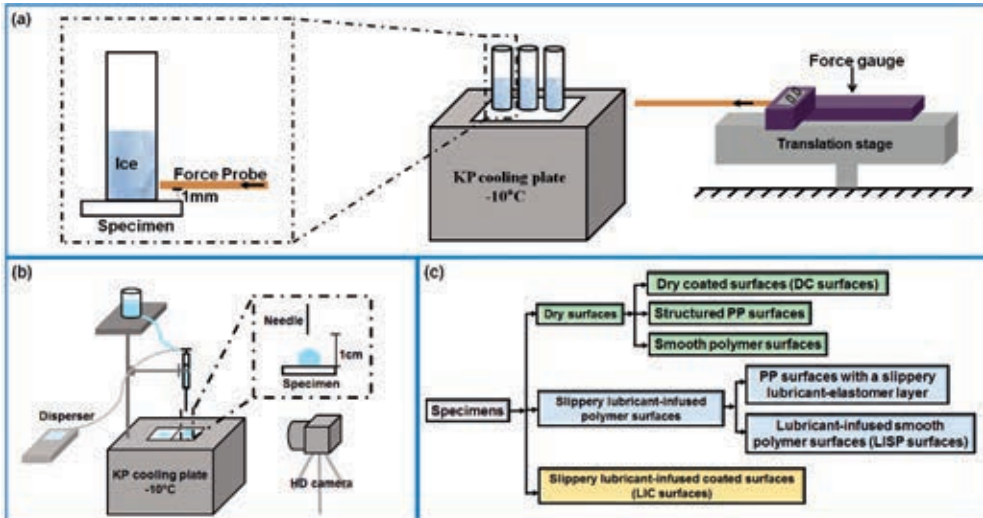


Figure 20. (a) Schematic of ice adhesion shear strength test process. The scheme is not drawn to scale. (b) Schematic of delayed ice nucleation test process. The scheme is not drawn to scale. (c) Classification of all surface materials.

## 3 RESULTS AND DISCUSSION

### 3.1 DRY SURFACES

#### 3.1.1 Surface properties

The morphologies of the dry rod-coated surfaces are shown in [Figures 21 a-c](#). Scanning electron microscope (SEM) images of the respective DC surfaces reveal that substrates covered with dense uniform overlayers. As the concentration of SiO<sub>2</sub> NPs increases, the structures of the DC surfaces become more compact. The DC-6 surface exhibits the highest roughness; on this surface, a hierarchical structure of individual spherical SiO<sub>2</sub> NPs (16-25 nm) and their micro-scaled aggregates (0.2-5 μm), which induces superhydrophobicity, has formed.

The morphologies of the respective structured PP surfaces are shown in [Figures 21 d-f](#). The MPP surface comprises evenly distributed micro-pillars with 20- $\mu\text{m}$  diameters, heights, and spacings. The NPP surface comprises irregularly distributed nano-pillars with diameters of 40-76 nm. The MNPP surface comprises a hierarchical structure formed by regular micro-pillars and irregular nano-pillars. The nano-pillars are superimposed over the entire surfaces of the micro-pillars and the base surfaces between micropillars.

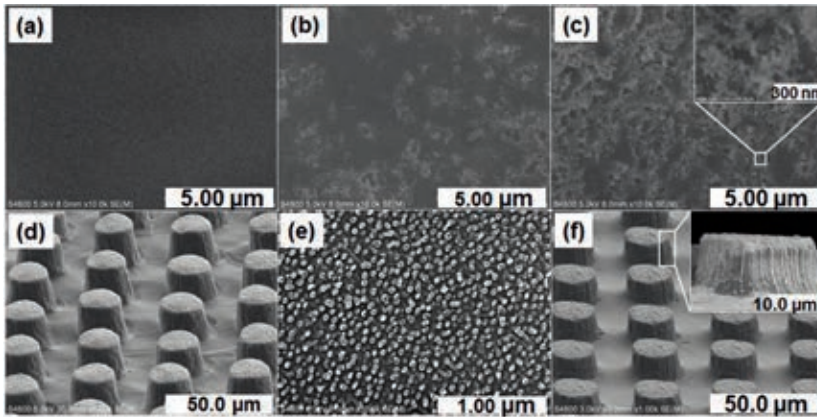


Figure 21. SEM images of surface morphologies on samples (a) DC-0, (b) DC-2, (c) DC-6, (d) MPP, (e) NPP, and (f) MNPP. ([Publication I](#))

The wettability and surface energy of each rod-coated, structured PP, and smooth polymer surface are listed in [Table 2](#).

Table 2. Static water (WCA), advancing (ACA), and receding (RCA) contact angles, contact angle hysteresis (CAH), and surface energies of dry surfaces. ([Publication I](#))

Specimen	WCA	ACA	RCA	CAH	Surface energy
Al substrate	55±1°	57±3°	31±3°	27±6°	39.0 mJ/m <sup>2</sup>
DC-0	103±1°	110±1°	90±1°	20±1°	30.0 mJ/m <sup>2</sup>
DC-1	109±1°	116±1°	89±1°	28±1°	25.6 mJ/m <sup>2</sup>
DC-2	123±1°	127±2°	102±2°	25±1°	24.0 mJ/m <sup>2</sup>
DC-3	137±1°	144±2°	123±4°	23±2°	21.6 mJ/m <sup>2</sup>
DC-4	149±1°	162±2°	136±3°	27±4°	20.0 mJ/m <sup>2</sup>
DC-5	162±2°	163±5°	148±3°	14±8°	18.9 mJ/m <sup>2</sup>
DC-6	167±1°	165±3°	155±3°	10±2°	18.6 mJ/m <sup>2</sup>
SPP	102±2°	111±2°	89±2°	22±1°	29.5 mJ/m <sup>2</sup>
NPP	128±7°	132±14°	107±14°	24±1°	28.6 mJ/m <sup>2</sup>
MPP	147±5°	154±4°	121±8°	33±4°	22.1 mJ/m <sup>2</sup>
MNPP	151±6°	158±9°	128±7°	30±2°	20.5 mJ/m <sup>2</sup>
STHV	103±1°	112±6°	92±6°	20±8°	26.0 mJ/m <sup>2</sup>
SPE	94±8°	108±1°	85±3°	23±3°	30.9 mJ/m <sup>2</sup>
SMPR	100±4°	106±1°	72±2°	34±3°	33.0 mJ/m <sup>2</sup>
SPC	88±1°	94±3°	65±4°	29±6°	35.2 mJ/m <sup>2</sup>
PES-0	80±1°	101±2°	64±1°	37±3°	35.4 mJ/m <sup>2</sup>
SPMMA	86±3°	85±4°	56±1°	30±4°	39.8 mJ/m <sup>2</sup>

The introduction of low-surface-energy ( $30.0 \text{ mJ/m}^2$ ) PVDF to the DC surfaces has rendered their rod-coated surfaces hydrophobic; as the concentration of  $\text{SiO}_2$  NPs increases, the WCA increases from  $103^\circ$  to  $167^\circ$ . The DC-5 and DC-6 surfaces are superhydrophobic with WCAs of  $162 \pm 2^\circ$  and  $167 \pm 1^\circ$ , respectively. The CAH values of DC-5 and DC-6 are  $14^\circ$  and  $10^\circ$ , respectively, indicating that DC-5 is a petal surface with a Cassie-Wenzel transition state and DC-6 is a lotus surface with a Cassie-Baxter state.[13,91,92] While water dropped onto the DC-6 surface easily slipped off, water droplets adhered to DC-5 surface even after it was turned over, confirming that the superhydrophobic DC-5 is a petal surface.

Because the surface energy of SPP is  $29.5 \text{ mJ/m}^2$ , all structured PP surfaces are hydrophobic. Introduction of nano- and micro-structures to the PP surfaces increased their WCAs to  $128^\circ$  and  $147^\circ$ , respectively. The WCA and CAH values of MNPP are  $151^\circ$  and  $30^\circ$ , respectively, indicating that the superhydrophobic MNPP is a petal surface.[13]

### 3.1.2 Icephobic performance

To clarify the icephobic performance of the dry surfaces, several observational techniques were used to measure  $\tau_{\text{ice}}$ , defined as the ratio of peak force during fracturing to the cross-sectional ice-surface contact area ( $\pi \times 9^2 \text{ mm}^2$ ), the freezing delay time ( $t_a$ ), and the freezing point at  $-10^\circ \text{C}$ . Rime ice was formed to simulate the ice produced in clouds and fog.[130] If no ice debris formed on a surface, it had an adhesive fracture mode; if ice debris partially formed on a surface, ice-surface and ice-ice fractures occurred (mixed mode); if full ice debris formed on a surface, it had a cohesive fracture mode.[45,66]

Figure 22a shows a plot of  $\tau_{\text{ice}}$  for the rod-coated and structured PP surfaces against their CAH values. Except for DC-5, DC-6, and MPP in adhesive mode, the  $\tau_{\text{ice}}$  values have a positive linear correlation with CAH, as proposed by Kulinich et al.[68]

For the DC surfaces, DC-0 has the lowest  $\tau_{\text{ice}}$  value at  $109 \text{ kPa}$ . As the surface roughness and hydrophobicity increase, the  $\tau_{\text{ice}}$  values of the rough Wenzel-state DC-1, DC-2, DC-3, and DC-4 all increase as a result of the mechanical interlocking effect between the ice and surfaces based on the electrostatic and Van der Waals forces. In these cases, the water completely penetrated the surface textures, enhancing the ice-surface contact area.[63,131,132] Accordingly, increasing the roughness of the Wenzel-state surfaces increases the value of  $\tau_{\text{ice}}$ .

Although DC-5 and DC-6 have lower values of  $\tau_{\text{ice}}$  than the rough Wenzel-state surfaces, their values are larger than that of the smooth DC-0. This indicates that, for SHSs with a heterogeneous wetting state, the value of  $\tau_{\text{ice}}$  is simultaneously controlled by the mechanical interlocking effect and stress concentrators with the mechanical interlocking effect dominating the ice adhesion. The stress concentrator is a counterforce generated by the compressive force of ice with sealed air cushions in the TCL and the microcracks appearing at the edges of the microstructures acting

as the stress concentrators.[131,133] The effect of stress concentrator is greater on the lotus surface than on the petal surface.

There is no significant difference between the  $\tau_{ice}$  values of the SPP and NPP surfaces, indicating that the mechanical interlocking effect on the NPP surface is relatively low. The overall trend in the value of  $\tau_{ice}$  on the structured PP surfaces is MNPP > MPP > NPP  $\approx$  SPP.

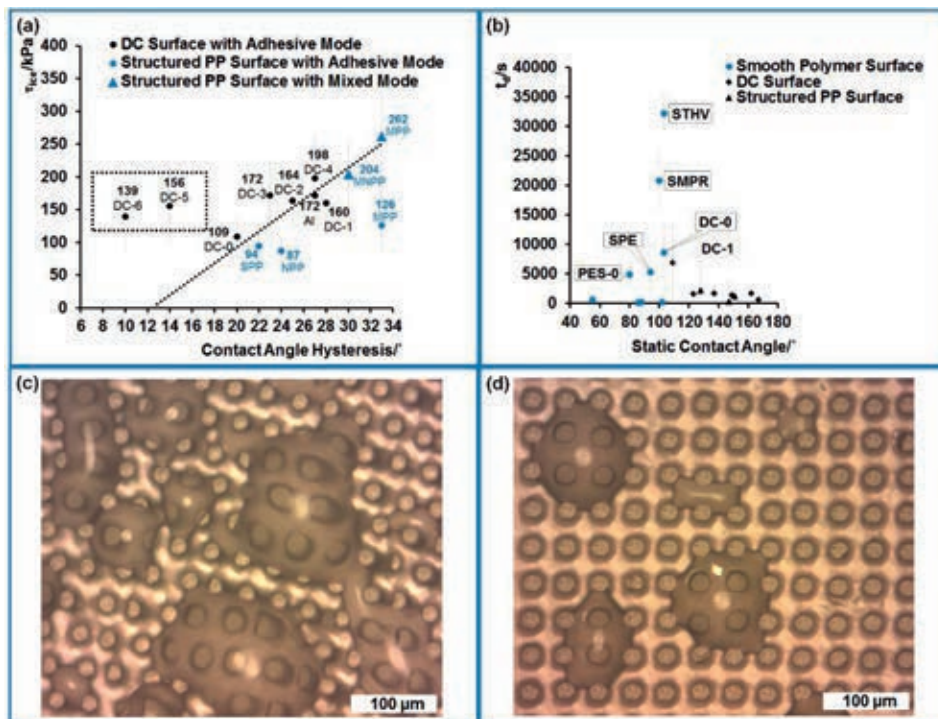


Figure 22. (a) Ice adhesion shear strength ( $\tau_{ice}$ ) as a function of CAH values of dry rod-coated and structured PP surfaces. The fracture modes are adhesive mode/mixed mode. (b) Freezing delay time ( $t_d$ ) as a function of WCA values of dry surfaces. (c) Optical microscope images of water condensation on MPP at -10 °C. (d) Optical microscope images of water condensation on MNPP at -10 °C. (Publication I )

Figure 22b shows the freezing delay times ( $t_d$ ) of the dry surfaces during the ice nucleation testing at -10 °C, where  $t_d$  is defined as the length of time from the dripping of a water droplet onto the surface to the onset of nucleation.

The values of  $t_d$  for the lotus surface of DC-6 and the petal surfaces of DC-5 and MNPP were all relatively small at 600s, 1800s, and 1200s, respectively, possibly as a result of the condensation of water in the sub-zero environment.[131,133] Water condensation at -10 °C was confirmed through direct observation of an optical microscope. Figures 22c-d show large numbers of microdroplets condensed onto the MPP and MNPP at -10 °C. The poor humidity tolerance of the SHSs under sub-zero conditions induced the water to penetrate the textures, increasing the water-surface

contact area and the amount of heat exchange, which in turn induced the SHSs to lose their superhydrophobicity and lower the value of  $t_a$ .<sup>[132–134]</sup> By contrast, the freezing points of DC-2 and NPP were  $-25.8\text{ }^\circ\text{C}$  and  $-26\text{ }^\circ\text{C}$ , respectively.

The values of  $t_a$  of supercooled water droplets on STHV, SMPR, and DC-0 were significantly higher than those of the state-of-the-art icephobic materials ( $\sim 7220\text{s}$ ).<sup>[63]</sup> The  $t_a$  of STHV, SMPR, and DC-0 are about 9h, 6h, and 8641s, respectively. The insulation effect of smooth low-density polyethylene resin (SMPR) and the strong freezing suppression of the smooth fluorinated surfaces (STHV and DC-0) inhibited ice nucleation.<sup>[135,136]</sup> The high  $t_a$  values of these materials are also attributable to their smooth and chemically homogeneous surfaces, which have higher energy barriers and fewer potential sites for heterogeneous ice nucleation.<sup>[137,138]</sup>

Based on the ice adhesion results reported above, we conclude that smooth hydrophobic surfaces are promising icephobic materials candidates.

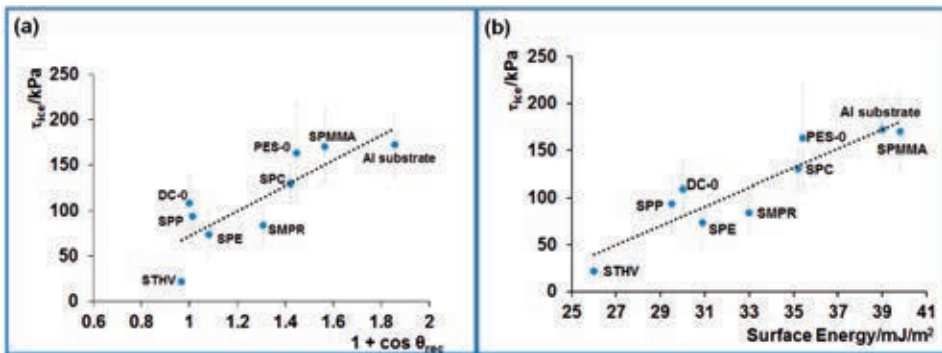


Figure 23. (a) Ice adhesion shear strength ( $\tau_{ice}$ ) as a function of  $(1 + \cos\theta_{rec})$  for nine smooth surfaces in adhesive mode. (b) A plot of  $\tau_{ice}$  against intrinsic surface energy for nine smooth surfaces in adhesive mode. (Publication I)

To verify the role of wettability and surface energy of smooth surfaces on the  $\tau_{ice}$ , nine types of smooth hydrophobic surfaces were fabricated. A plot of  $\tau_{ice}$  against  $(1 + \cos\theta_{rec})$  is shown in Figure 23a. A linear correlation exists between the  $\tau_{ice}$  values and the parameter  $(1 + \cos\theta_{rec})$  on the nine smooth surfaces, confirming the findings of Meuler et al.<sup>[55]</sup>

A linear correlation is also observed between the  $\tau_{ice}$  values and the intrinsic surface energy ( $E$ ), (Figure 23b) following the empirical relationship  $\tau_{ice} = 10E - 224$ . The low surface energies of the smooth surfaces generate low ice adhesion, in agreement with the proposal of Ozbay et al.<sup>[67,131]</sup> The low ice adhesion on low-surface-energy surfaces is driven by the decrease in the density of water at the water-surface interface. This density-reduction layer, which ranges in thickness from 0.1 nm to 1 nm, can weaken the Van der Waals force at the water/ice-surface. The thickness of the density-reduction layer is inversely proportional to  $\tau_{ice}$  and proportional to the WCA. Increasing the WCA and reducing surface energy will reduce  $\tau_{ice}$ .<sup>[45]</sup>

The STHV sample, which had low surface energy ( $26.0 \text{ mJ/m}^2$ ), was found to have the lowest ice adhesion of  $22 \pm 13 \text{ kPa}$ , being approximately eight times lower than that of the Al substrate. This suggests that STHV is a potentially icephobic material with low ice adhesion and long freezing delay time ( $\sim 9\text{h}$ ).

## 3.2 SLIPPERY LUBRICANT-ELASTOMER INFUSED POLYMER SURFACES

### 3.2.1 Surface properties

The morphologies and side geometries of high-aspect-ratio PP surfaces are shown in [Figures 24a-c](#). The CC surface comprises regularly arranged high-aspect-ratio micro-pits. The dimensions of the CC surface are  $a_c = 85 \text{ }\mu\text{m}$ ,  $b_c = 40 \text{ }\mu\text{m}$ ,  $c_c = 55 \text{ }\mu\text{m}$ ,  $d_c = 115 \text{ }\mu\text{m}$ , and  $H_c = 350 \text{ }\mu\text{m}$ . The OC surface is a regular array of high-aspect-ratio barrel-shaped micro-pillars and has the dimensions  $a_o = 30 \text{ }\mu\text{m}$ ,  $b_o = 75 \text{ }\mu\text{m}$ ,  $c_o = 65 \text{ }\mu\text{m}$ ,  $d_o = 30 \text{ }\mu\text{m}$ , and  $H_o = 120 \text{ }\mu\text{m}$ .

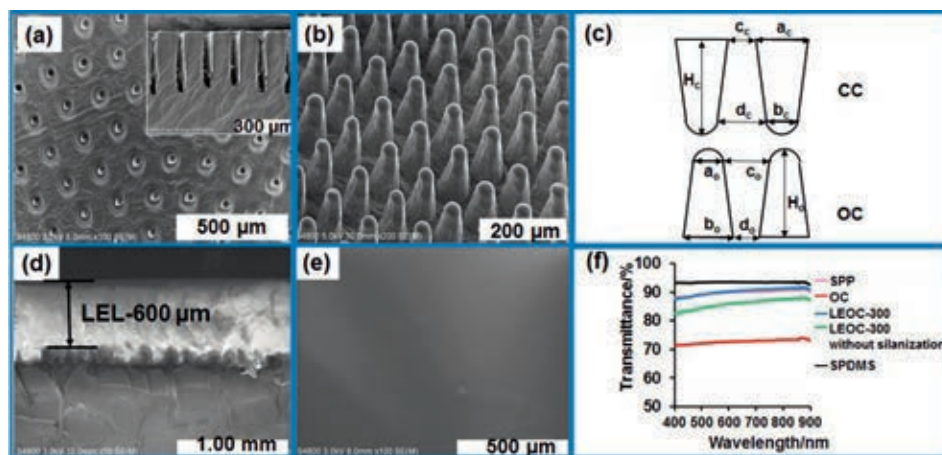


Figure 24. SEM images of surface morphology of (a) high-aspect-ratio CC ( $\sim 6:1$ ) with micro-pits, (b) high-aspect-ratio OC ( $\sim 3:1$ ) with micro-pillars, (c) lateral geometries of CC and OC, (d) side view of LEOC-600, and (e) LESPP-600. (f) UV-Vis transmittance spectra. ([Publication II](#))

Original PP surfaces were infiltrated with  $300\text{-}\mu\text{m}$  and  $600\text{-}\mu\text{m}$  LELs to produce slippery LISSs. In the fabrication process, SEM was used to verify the thickness of the LELs, which was defined as the distance between the tops of the structure and the LEL ([Figure 24d](#)). [Figure 24e](#) shows the smooth topography of the LESPP-600 surface, which disagrees with the wave-like topography of lubricant-infused polymer surfaces reported in Coady et al.[\[139\]](#)

To confirm the importance of the LEL to the rough surface and silanization effects, the transparencies of SPP, OC, SPDMS, LEOC-300, and LEOC-300 without silanization were measured. ([Figure 24f](#)) The transmittance of OC was  $\sim 73\%$  in the

visible and near-infrared light regions, while that of LEOC-300 increased to ~ 91.5%, a value close to that of SPP, at a wavelength of 800 nm. These results indicate that the infiltration of the LEL has made the translucent OC transparent. The mechanism for this arises from the solid-air interface at the superhydrophobic OC surface, which induces irregular reflections that reduce the transmittance. The LEL that infiltrates these air pockets has a reflection index similar to that of the SPP, which significantly increases the transmittance.[140,141] However, the transparency of LEOC-300 without silanization is only ~ 87.5% at 800 nm; the difference between the transmittances of LEOC-300 and LEOC-300 without silanization proves that the silanization process allows the LICLE solution to completely wet the structured PP. As a confirmation, SEM imaging revealed no phase separation within the LISSs.

The wettabilities of all of the original polymer surfaces and the LISSs are listed in Table 3. The WCA of SPP is ~ 102°, indicating that it is hydrophobic. The introduction of high-aspect-ratio micro-pits and micro-pillars increases the WCA to ~ 119° and ~ 160°, respectively. The CAH of OC is ~ 14°, indicating that the OC surface is a petal surface in a Cassie-Wenzel transition state.[13]

Table 3. Static water (WCA), advancing (ACA), and receding (RCA) contact angles, and contact angle hysteresis (CAH) of original polymer surfaces and LEL infused surfaces at room temperature and -10 °C. (Publication II)

Specimen	Room temperature				-10°C
	WCA	ACA	RCA	CAH	WCA
SPDMS	114±1°	122±1°	94±2°	28±2°	-
SPP	102±2°	111±2°	89±2°	22±1°	98±2°
CC	119±4°	126±6°	96±5°	30±1°	89±3°
OC	160±3°	159±2°	145±1°	14±1°	122±8°
LESPP-300	105±3°	108±2°	103±1°	6±2°	-
LECC-300	110±1°	107±2°	105±2°	2±1°	-
LEOC-300	109±1°	108±2°	103±3°	5±5°	-
LESPP-600	105±3°	108±1°	103±2°	6±2°	-
LECC-600	110±1°	108±2°	102±5°	7±7°	-
LEOC-600	109±1°	108±1°	104±1°	4±1°	-

There is no significant difference between the WCAs of the SPP at room temperature and under a cold environment at -10 °C. This indicates that a cold environment has little effect on the smooth surface. By contrast, the WCAs of CC and OC decrease to ~ 89° and ~ 122° at -10 °C, respectively. The OC surface loses its superhydrophobicity in the cooling process, indicating that condensed water penetrates and propagates through its structures.

The complete encapsulation the PP surfaces by the LEL significantly changes both the WCA and CAH of these surfaces, with the WCA values dropping to 105° - 110° and all of CAH values falling to below 10°. These low CAH values confirm the ultra-smooth surface characteristics and the complete elimination of pinning points.[69] Varying the thickness and surface structures of the LISSs had no significant effect on the wettability of their surfaces.

### 3.2.2 Icephobic performance

To produce a durable, icephobic LISS through a simple one-step-procedure, a low-surface-energy PDMS elastomer with a 3D cross-linking network was used to lock in the silicone oil. The PDMS elastomer was chosen based on an application of Kendall and Chaudhury's equation, in which large differences between the moduli of ice and soft elastomer cause a mismatch in strains under stress, which in turn leads to low ice adhesion.[60,76,127,142]

From Figure 25, it is seen that the SPP surface has a lower ice adhesion than the structured PP surfaces with high aspect ratios, in agreement with previous reports.[65,66] The structured PP surfaces with high aspect ratios have the highest ice adhesions among the original polymer surfaces and the LISSs. The high ice adhesion of the CC surface is a result of a slight hydrophobicity that induces a Wenzel state, resulting in mechanical interlocking and a larger contact area. The OC surface, in turn, has a larger ice adhesion than the CC surface because the OC surface, which is an SHS at room temperature, assumes a Wenzel state as a result of water condensation at  $-10\text{ }^{\circ}\text{C}$ . This results in a larger contact area and a stronger mechanical interlocking than on the CC surface.[66,113,132]

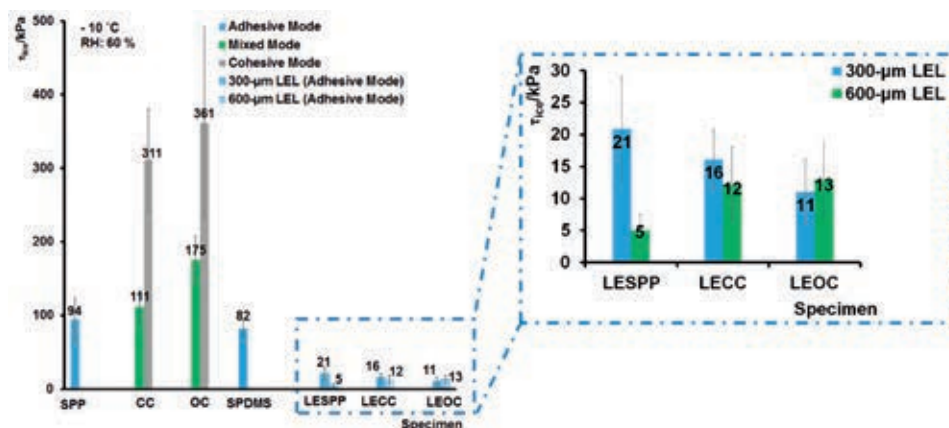


Figure 25. Ice adhesion shear strength ( $\tau_{ice}$ ) of original polymer surfaces and lubricant-elastomer infused polymer surfaces. (Publication II)

The infusion of an LEL significantly reduces the  $\tau_{ice}$  of all of the LISSs. The  $\tau_{ice}$  values of the skin-like LISSs are an order of magnitude lower than those of the original PP surfaces, while the LEL-infused LISSs attain ultra-low values of  $\tau_{ice}$  of down to  $\sim 5\text{ kPa}$ . As accreted ice can be self-removed by a strong breeze by a threshold of  $\sim 55\text{ kPa}$ ,[31] strong breeze can self-remove the accreted ice on all of the LEL-infused LISSs. The significantly reduced contact areas between the ice and the matrix in LEL-infused LISSs account for their low  $\tau_{ice}$  values. The reduced contact areas, in turn, are a result of molecular homogeneity, low CAH values, the low



surface energies of the PDMS and silicone oil, the presence of the oil layer, and the mismatch between the strains of the ice and the soft PDMS elastomer.[27,76,114]

To confirm the effects of the underlying structures of LEL-infused LISSs on their icephobic performance, the different underlying structures with thicknesses of 300  $\mu\text{m}$  and 600  $\mu\text{m}$  were prepared and tested.

Adding structured PP surfaces with high aspect ratios to 300- $\mu\text{m}$  LELs reduced their ice adhesion relative to that of smooth PP, with reductions of 48% and 24% obtained for OC and CC surfaces, respectively.

In the 600- $\mu\text{m}$  LEL case, however, the smooth PP had the lowest ice adhesion, and changing the LEL thickness of structured PP had little effect on ice adhesion. In addition, the ice adhesion of smooth PP with an LEL decreased as the LEL thickness increased, a trend consistent with the results of Wang et al. and Beemer et al.[60,103] Furthermore, the ultra-low ice adhesion of the LESPP-600 surface ( $\sim 5$  kPa) indicates that the minimum roughness is not necessary for the effective immobilization of the lubricant on the matrix, disagreeing the previous reports.[69,70,140,143,144]

Figure 26a shows that at  $-10$   $^{\circ}\text{C}$  and a  $16^{\circ}$  slope, 100- $\mu\text{L}$  aqueous droplets form initially at the edges of the original PP surfaces. After 5 min, the supercooled aqueous droplets are still stuck to the original PP surfaces. By contrast, all the LEL-infused LISSs demonstrate extraordinary dynamic mobility at  $-10$   $^{\circ}\text{C}$ ; the sliding times ( $S_t$ ) of the supercooled aqueous droplets on each surface are shown in Figure 26b. The LEL-infused LISSs remain clean after shedding the aqueous droplets, indicating that the LISSs have an anti-dust property.

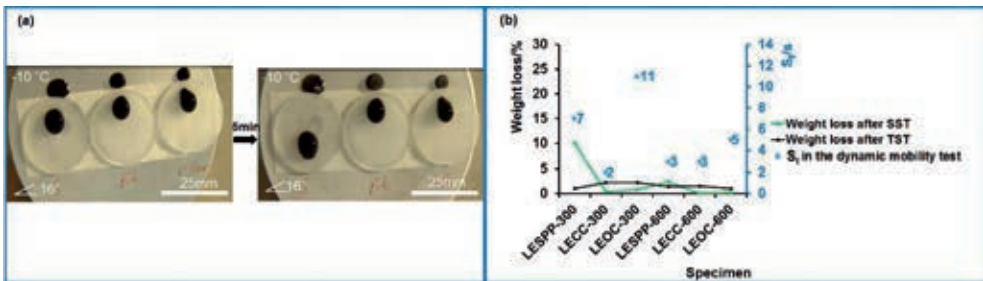


Figure 26. (a) Image showing dynamic mobility behavior of 100- $\mu\text{L}$  aqueous droplets on SPP, CC, and OC at a  $16^{\circ}$  slope and  $-10$   $^{\circ}\text{C}$ . As anti-dust indicators, the aqueous droplets contain 10 wt% synthesized diamond nanoparticles. (b) Weight loss following shear stability test (SST) and thermal stability test (TST) and sliding times ( $S_t$ ) under the dynamic mobility test. (Publication II)

The liquid lubricants assessed in previous studies were immobilized only by the surface roughness through the action of capillary force and chemical affinity. Liquid lubricants that directly infuse into a structure easily evaporate and lose their slippery properties.[122,128,145–147] To determine the shear stability of the lubricants applied in this study, the weight losses in the respective samples were measured following spinning at 3500 rpm for one minute. The weight losses reflect the amount

of silicone oil is removed. It is seen from Figure 26b that most of the LEL-infused LISSs had weight losses of less than 3% and that, although the weight loss of the LESPP-300 sample was around 10%, its CAH remained below 10°. The low CAHs on the surfaces are an indicator of their slippery properties and ice repellency.[68]

After 168 hours of thermal stability testing at 70 °C, the weight losses and CAHs of all LISSs remained below 3% and 10°, respectively, and all LISSs remained slippery after more than 360 days in an ambient environment.

It was seen from Figure 27a that the CAHs of the LESPP-300, LECC-300, LEOC-300, and LESPP-600 samples remained below 10° following 50-cycle abrasion testing. The values of  $\tau_{ice}$  of the surfaces also remained unchanged. (Figure 27b) These low CAHs and unchanged ice adhesion values indicate that the LEL-infused LISSs were mechanically robust.

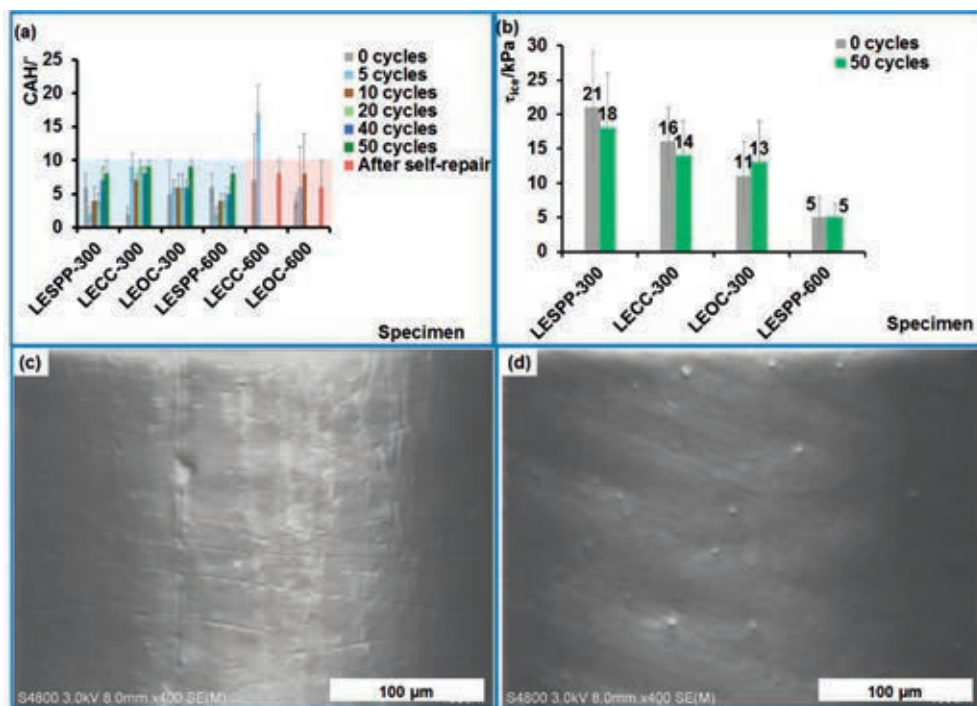


Figure 27. (a) CAH of LISS following abrasion cycles and self-repair. (b) Ice adhesion shear strength ( $\tau_{ice}$ ) of LISSs with robust mechanical stability following abrasion cycles. (c) SEM image of LEOC-600 following 10 abrasion cycles. (d) SEM image of LEOC-600 following self-repair. (Publication II)

By contrast, the CAH values of LECC-600 and LEOC-600 exceeded 10° following five cycles of abrasion testing. These increased CAH values indicate a loss of lubricant or damage to the ultra-smooth surface. The damages to the LEOC-600 surface, on which scratches appeared after ten abrasion cycles, is shown in Figure 27c.

After heating to 80 °C, the damaged LECC-600 and LEOC-600 recovered their water repellency after 30 min and 5 min, respectively. After the thermal stimulus, the CAHs of LECC-600 and LEOC-600 are  $8\pm 2^\circ$  and  $6\pm 4^\circ$ , respectively. This recovery of slippery properties indicates that self-repair followed the thermal stimulus, an effect that was verified by the SEM observations. Figure 27d shows the healed, smooth LEOC-600 surface following self-repair.

### 3.3 SLIPPERY LUBRICANT-INFUSED COATED SURFACES

#### 3.3.1 Surface properties

Several systematic studies were carried out to investigate the effects of silicone oil and silica nanoparticle ( $\text{SiO}_2$  NP) content on the wettability, slippery behavior, and morphologies of lubricant-infused coated surfaces. Figures 28a-b show surface plots of WCA and CAH as functions of silicone oil (x-axis) and  $\text{SiO}_2$  NP content (y-axis). These results demonstrate how wettability can be tuned through the enhancement of silicone oil content and/or  $\text{SiO}_2$  NP content.

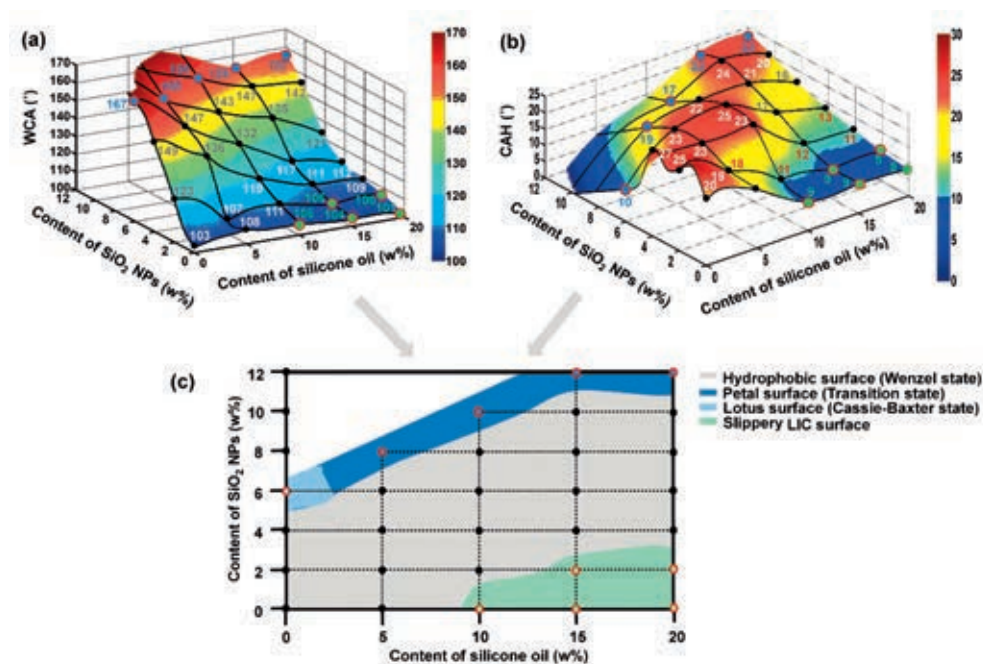


Figure 28. 3D plots of surface wettability as functions of silicone oil and silica nanoparticle ( $\text{SiO}_2$  NP) content, showing (a) static water contact angle (WCA) and (b) contact angle hysteresis (CAH). (c) Grid map of wetting behavior based on oil and  $\text{SiO}_2$  NP content. (Publication III)

It is seen from [Figure 28a](#) that, in the absence of silicone oils, the WCA of the LIC surfaces gradually increases as the SiO<sub>2</sub> NP content increases. An SHS eventually is obtained at WCA and CAH values of 167° and 10°, respectively. This LIC-0-6 surface is a lotus structure in a Cassie-Baxter state.[\[13\]](#) The rough hierarchical micro-nano-structures of the LIC-0-6 surface, shown in [Figure 29a](#), also verify its superhydrophobic properties. The 3D porous interconnected network of the LIC-0-6 comprises micro-clusters (0.2-5 μm) and micro-pores formed by the aggregation of spherical SiO<sub>2</sub> NPs (16-25 nm).[\[66\]](#)

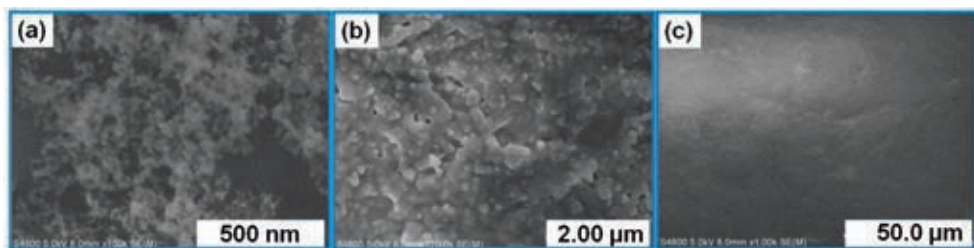


Figure 29. SEM images of (a) LIC-0-6, (b) LIC-20-12, and (c) LIC-20-2. ([Publication III](#))

To ensure environmentally friendly coatings, different contents of silicone oil are added to create a slippery surface. Here, the added silicone oil content was varied over the range 5 wt%, 10wt%, 15 wt%, and 20 wt%, while the added SiO<sub>2</sub> NPs content was varied from 0 wt% to 12 wt% in 2-wt% intervals. As a constant silicone oil content, increasing the SiO<sub>2</sub> NPs content increased the WCA of the LIC surfaces until an SHS appeared, as occurred in the oil-free surfaces. However, in the presence of silicone oil all of the SHSs (marked with blue points in the figure), had CAH values of greater than 10°. This indicates that the LIC-5-8, LIC-10-10, LIC-15-12, and LIC-20-12 surfaces were all petal surfaces in Cassie-Wenzel transition states.[\[13,148\]](#) SEM imaging of the LIC-20-12 revealed that the silicone oil was only partially present and hierarchical structures were remained to maintain the superhydrophobicity on the rough petal surfaces. ([Figure 29b](#))

Only at silicone oil content above 10 wt%, the addition of the lubricant to the slightly hydrophobic LIC surfaces significantly reduce the CAH and cause the appearance of slippery properties. The low CAH values of the slippery LIC-10-0, LIC-15-0, LIC-15-2, LIC-20-0, and LIC-20-2 surfaces (marked with green points in the figure) indicate that the surfaces are completely covered by silicone oil and have homogeneous liquid-liquid interfaces. There are no pinning points or SiO<sub>2</sub> NPs on the slippery surfaces.[\[69,115,149\]](#) This nearly defect-free surface morphology was verified through SEM imaging of the LIC-20-2 sample. ([Figure 29c](#)) By contrast, the WCAs of the slippery surfaces remained unchanged owing to their relatively unchanged morphologies and surface chemistries.[\[150\]](#)

Based on the results shown in [Figures 28a-b](#), an empirical grid map of wetting behaviors was constructed ([Figure 28c](#)). The wetting behavior regions include the

Wenzel-state hydrophobic, petal, lotus, and slippery surfaces. The map can be used to tune the wettability, slippery property, and surface morphology of a lubricant-infused coated surface.

### 3.3.2 Icephobic performance

Figure 30a shows the  $\tau_{ice}$  values of LIC surfaces with different silicone oil and SiO<sub>2</sub> NPs content. In all of the LIC surfaces, the SHSs have the highest  $\tau_{ice}$  values, which range from 102 kPa to 147 kPa. The high ice adhesion of the SHSs arises from their petal surfaces and Cassie-Wenzel states. At -10 °C, the poor humidity tolerance of the petal surfaces causes water to condense in the rough textures, resulting in an increased ice-matrix contact area and stronger mechanical interlocking.[13,66,148]

The values of  $\tau_{ice}$  on most of the LIC surfaces in the hydrophobic wetting region (marked with black points in the figure) are larger than the value (~55 kPa) that can be used to self-remove the accreted ice by a strong breeze,[31] indicating that ice accreted on such surfaces will not be easily self-removed by a strong breeze. However, the  $\tau_{ice}$  values of the LIC-5-0, LIC-10-2, and LIC-15-4 surfaces are slightly lower than 55 kPa in the hydrophobic wetting region because they have fewer SiO<sub>2</sub> NPs and more silicone oil, which reduces the ice-matrix contact area.

It is seen from Figure 30a that the  $\tau_{ice}$  values of all of the LIC surfaces in the slippery wetting region (LIC-10-0, LIC-15-0, LIC-15-2, LIC-20-0, and LIC-20-2: marked with green points in the figure) are an order of magnitude lower than those of the SHSs. These dramatic changes in the  $\tau_{ice}$  values of the SHSs, Wenzel-state rough surfaces, and slippery surfaces demonstrate the importance of slippery properties on icephobic performance. The low  $\tau_{ice}$  values of the slippery surfaces arise from their nearly defect-free surface morphologies and homogeneous liquid-liquid interfaces, which result in fewer pinning points, reduced contact area, and the formation of loose ice.[69,114,115]

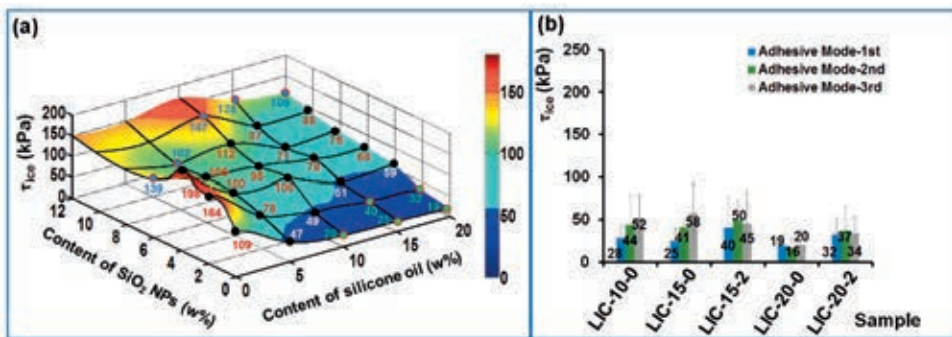


Figure 30. (a) Surface plot of ice adhesion shear strength ( $\tau_{ice}$ ) as functions of silicone oil and silica nanoparticle (SiO<sub>2</sub> NP) content. (b)  $\tau_{ice}$  of slippery coated surfaces following three cycles of icing/ice-detachment. (Publication III)

All the slippery surfaces retained their slippery properties after more than 360 days under an ambient environment. To determine the durability of the slippery coated surfaces, three-repeated icing/ice-detachment cycles (RIIDC) were conducted. (Figure 30b) Following the three RIIDC, the values of  $\tau_{ice}$  of the slippery surfaces with 10 wt% and 15 wt% silicone oil gradually increased, even being more than 55 kPa. By contrast, the  $\tau_{ice}$  values of the slippery surfaces with 20 wt% silicone oil remained essentially unchanged after three RIIDC. This indicates that the surfaces with 20 wt% silicone oil had the most durable icephobic performance.

To determine the role of SiO<sub>2</sub> NPs in slippery behavior and icephobicity, a lubricant shear stability test was conducted on several 20 wt% silicone-oil-infused slippery surfaces. After spinning at 3500 rpm for 1 min, the LIC-20-0 and LIC-20-2 surfaces experienced weight losses of 17.0% and 0.6%, respectively. The role of the SiO<sub>2</sub> NPs is to firmly anchor the oil overlayer and prevent the adsorption of contaminants by drying the surface.

The average freezing point of the LIC-20-2 surface was  $-27.1 \pm 0.7$  °C, as compared to the freezing points of reference surfaces (Al substrate and LIC-0-0) of  $-21.6$  °C and  $-24.4$  °C, respectively.[66] The delayed ice nucleation of the LIC-20-2 surface arises from: i) the low CAH; ii) the weak intermolecular forces between the nonpolar silicone oil and the polar water; and iii) the cloaking behavior of water droplets in the silicone oil.[145,151]

To determine the effect of surface energy on the values of  $\tau_{ice}$  in slippery surfaces, eight LISP surfaces with an optimal 20 wt% silicone oil content were fabricated. Figure 31 shows that the introduction of silicone oil to a polymer STHV with a surface energy of 26 mJ/m<sup>2</sup> did not lower the  $\tau_{ice}$  value. However, polymers with initial surface energies at or above 29.5 mJ/m<sup>2</sup> caused reductions in  $\tau_{ice}$  values following the introduction of silicone oil. The 20 wt% silicone-oil-infused SPP, DC-0, and SPE surfaces all had extremely low ice adhesions. These results indicate that the infusion of silicone oil into polymers with surface energies ranging from 29 to 31 mJ/m<sup>2</sup> can potentially reduce the ice adhesion.

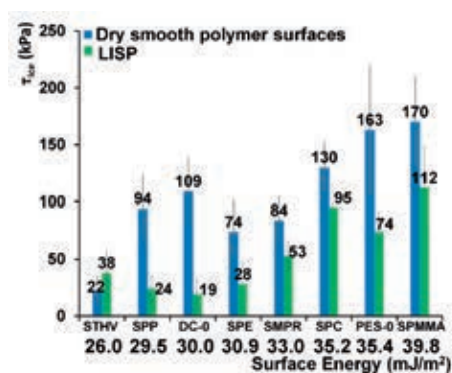


Figure 31. Ice adhesion shear strength ( $\tau_{ice}$ ) of dry smooth polymer and slippery lubricant-infused smooth polymer (LISP) surfaces as a function of surface energy. (Publication III)

## 4 CONCLUSIONS

In this study, dry rod-coated, structured polypropylene (PP), smooth polymer, and lubricant-elastomer infused polymer surfaces were developed along with one-step silicone-oil-infused slippery coatings. The effects of wettability, surface energy, structuring, and lubricant-infused layer on icephobic performance were explored.

Dry surfaces that exhibit rough Wenzel-state hydrophobicity were found to have significantly enhanced ice adhesion ( $\tau_{ice}$ ) relative to smooth references. This arises from mechanical interlocking in the textures, with the value of  $\tau_{ice}$  increasing with roughness. In superhydrophobic surfaces (SHSs), including petal and lotus surfaces, mechanical interlocking and stress concentrators control the  $\tau_{ice}$ . Neither petal nor lotus surfaces are icephobic due to poor thermal stabilities and humidity tolerances and enhanced contact areas under condensation environments. Except for the SHSs, there is a positive linear correlation between  $\tau_{ice}$  and contact angle hysteresis (CAH). A linear correlation was also found between  $\tau_{ice}$  and the scaling parameter of receding contact angle, with  $\tau_{ice}$  decreasing as the surface energy of smooth surfaces decreases. This suggests that simple, inexpensive, and mass-producible low-surface-energy smooth surfaces are promising for anti-icing applications.

The lubricant-elastomer infused polymer surfaces were found to have very low CAH and  $\tau_{ice}$  values compared to those of SHSs and dry smooth surfaces. Transparent lubricant-elastomer infused polymer surfaces were also found to have exceptional shear stability, evaporation resistance, anti-dusting, mechanical stability, and self-repairing. Adding a 300- $\mu\text{m}$  lubricant-elastomer layer (LEL) can reduce the  $\tau_{ice}$  of a structured PP surface by 24-48% relative to a smooth surface. Increasing the thickness of the LEL has no obvious change in the  $\tau_{ice}$  of closed-cell or open-cell structures. Increasing the thickness of LEL on a smooth PP surface reduces its  $\tau_{ice}$ , and a smooth PP surface with a 600- $\mu\text{m}$  LEL has an extremely low  $\tau_{ice}$  of 5 kPa, indicating that roughness is not required to maintain slippery properties. The simple one-step production strategy on a variety of smooth materials is inexpensive and widely applicable for icephobic applications.

We also developed a grid map of wetting behavior of silicone-oil-infused slippery coatings to tune wettability, morphology, and slippery property. The addition of silicone oil to a slightly hydrophobic coated surface can produce slippery properties and low  $\tau_{ice}$  that are an order of magnitude lower than SHSs. Superhydrophobic lubricant-infused surfaces have the highest  $\tau_{ice}$ . These results confirm that slippery properties are critical for icephobic applications. 20 wt% slippery silicone-oil-infused surfaces have the best icephobic performance and that the presence of nanoparticles effectively immobilizes the lubricant and imparts surface dryness to prevent contamination. The infusion of silicone oil into smooth polymers with surface energies ranging from 29 to 30  $\text{mJ}/\text{m}^2$  can produce low  $\tau_{ice}$ . Eco-friendly, one-step slippery coatings have great potential in icephobic applications.

## 5 BIBLIOGRAPHY

- [1] X. Yao, Y. Song, L. Jiang, Applications of bio-inspired special wettable surfaces, *Adv. Mater.* 23 (2011) 719–734.
- [2] M. Barberoglou, E. Stratakis, V. Zorba, E. Spanakis, P. Tzanetakis, S.H. Anastasiadis, C. Fotakis, Laser structured biomimetic artificial surfaces that quantitatively reproduce the water repellency of a lotus leaf, *CLEO/Europe - EQEC 2009 - Eur. Conf. Lasers Electro-Optics Eur. Quantum Electron. Conf.* (2009) 4049–4054.
- [3] J. Yong, F. Chen, Q. Yang, J. Huo, X. Hou, Superoleophobic surfaces, *Chem. Soc. Rev.* 46 (2017) 4168–4217.
- [4] X.Q. Feng, X. Gao, Z. Wu, L. Jiang, Q.S. Zheng, Superior water repellency of water strider legs with hierarchical structures: Experiments and analysis, *Langmuir.* 23 (2007) 4892–4896.
- [5] H. Zhu, Z. Guo, W. Liu, Adhesion behaviors on superhydrophobic surfaces, *Chem. Commun.* 50 (2014) 3900–3913.
- [6] X. Gao, L. Jiang, Water-repellent legs of water striders, *Nature.* 432 (2004) 36–36.
- [7] Y. Ding, S. Xu, Y. Zhang, A.C. Wang, M.H. Wang, Y. Xiu, C.P. Wong, Z.L. Wang, Modifying the anti-wetting property of butterfly wings and water strider legs by atomic layer deposition coating: Surface materials versus geometry, *Nanotechnology.* 19 (2008).
- [8] X. Gao, X. Yan, X. Yao, L. Xu, K. Zhang, J. Zhang, B. Yang, L. Jiang, The dry-style antifogging properties of mosquito compound eyes and artificial analogues prepared by soft lithography, *Adv. Mater.* 19 (2007) 2213–2217.
- [9] Z. Han, H. Guan, Y. Cao, S. Niu, L. Ren, Antifogging properties and mechanism of micron structure in *Ephemera pictiventris* McLachlan compound eyes, *Chinese Sci. Bull.* 59 (2014) 2039–2044.
- [10] Y. Song, Y. Liu, H. Jiang, Y. Zhang, J. Zhao, Z. Han, L. Ren, Mosquito eyes inspired surfaces with robust antireflectivity and superhydrophobicity, *Surf. Coatings Technol.* 316 (2017) 85–92.
- [11] W.R. Hansen, K. Autumn, Evidence for self-cleaning in gecko setae, *Proc. Natl. Acad. Sci.* 102 (2005) 385–389.
- [12] K. Liu, J. Du, J. Wu, L. Jiang, Superhydrophobic gecko feet with high adhesive forces towards water and their bio-inspired materials, *Nanoscale.* 4 (2012) 768–772.
- [13] L. Feng, Y. Zhang, J. Xi, Y. Zhu, N. Wang, F. Xia, L. Jiang, Petal Effect: A Superhydrophobic State with High Adhesive Force, *Langmuir.* 24 (2008) 4114–4119.
- [14] Y. Zheng, X. Gao, L. Jiang, Directional adhesion of superhydrophobic butterfly wings, *Soft Matter.* 3 (2007) 178–182.
- [15] G. Chen, Q. Cong, Y. Feng, L. Ren, Study On The Wettability And Self-cleaning Of Butterfly Wing Surfaces, *WIT Trans. Ecol. Environ.* 73 (2004) 245–251.
- [16] B.R. Wasik, S.F. Liew, D.A. Lilien, A.J. Dinwiddie, H. Noh, H. Cao, A. Monteiro, Artificial selection for structural color on butterfly wings and comparison with natural evolution, *Proc. Natl. Acad. Sci.* 111 (2014) 12109–12114.
- [17] S.H. Hong, J. Hwang, H. Lee, Replication of cicada wing's nano-patterns by hot embossing and UV nanoimprinting, *Nanotechnology.* 20 (2009).
- [18] G. Zhang, J. Zhang, G. Xie, Z. Liu, H. Shao, Cicada Wings: A Stamp from Nature for



- Nanoimprint Lithography, *Small*. 2 (2006) 1440–1443.
- [19] Y.F. Huang, Y.J. Jen, L.C. Chen, K.H. Chen, S. Chattopadhyay, Design for approaching cicada-wing reflectance in low- and high-index biomimetic nanostructures, *ACS Nano*. 9 (2015) 301–311.
- [20] A.R. Parker, C.R. Lawrence, Water capture by a desert beetle, *Nature*. 414 (2001) 33–34.
- [21] S. Jung, M. Dorrestijn, D. Raps, A. Das, C.M. Megaridis, D. Poulikakos, Are Superhydrophobic Surfaces Best for Icephobicity?, *Langmuir*. 27 (2011) 3059–3066.
- [22] J.L. Laforte, M.A. Allaire, J. Laflamme, State-of-the-art on power line de-icing, *Atmos. Res.* 46 (1998) 143–158.
- [23] J. Lv, Y. Song, L. Jiang, J. Wang, Bio-inspired strategies for anti-icing, *ACS Nano*. 8 (2014) 3152–3169.
- [24] J. Chen, Z. Luo, Q. Fan, J. Lv, J. Wang, Anti-Ice coating inspired by ice skating, *Small*. 10 (2014) 4693–4699.
- [25] L.E. Raraty, D. Tabor, The Adhesion and Strength Properties of Ice, *Proc. R. Soc. A Math. Phys. Eng. Sci.* 245 (1958) 184–201.
- [26] H.H. Jellinek, Adhesive properties of ice, *J. Colloid Sci.* 14 (1959) 268–280.
- [27] S. Zhang, J. Huang, Y. Cheng, H. Yang, Z. Chen, Y. Lai, Bioinspired Surfaces with Superwettability for Anti-Icing and Ice-Phobic Application: Concept, Mechanism, and Design, *Small*. 13 (2017) 1–20.
- [28] T.M. Schutzius, S. Jung, T. Maitra, P. Eberle, C. Antonini, C. Stamatopoulos, D. Poulikakos, Physics of Icing and Rational Design of Surfaces with Extraordinary Icephobicity, *Langmuir*. 31 (2015) 4807–4821.
- [29] K. Golovin, S.P.R. Kobaku, D.H. Lee, E.T. DiLoreto, J.M. Mabry, A. Tuteja, Designing durable icephobic surfaces, *Sci. Adv.* 2 (2016) e1501496.
- [30] V. Hejazi, K. Sobolev, M. Nosonovsky, From superhydrophobicity to icephobicity: Forces and interaction analysis, *Sci. Rep.* 3 (2013).
- [31] J. Chen, R. Dou, D. Cui, Q. Zhang, Y. Zhang, F. Xu, X. Zhou, J. Wang, Y. Song, L. Jiang, Robust prototypical anti-icing coatings with a self-lubricating liquid water layer between ice and substrate, *ACS Appl. Mater. Interfaces*. 5 (2013) 4026–4030.
- [32] M.J. Kreder, J. Alvarenga, P. Kim, J. Aizenberg, Design of anti-icing surfaces: smooth, textured or slippery?, *Nat. Rev. Mater.* 1 (2016) 15003.
- [33] M. Mohammadi, M. Tembely, A. Dolatabadi, Supercooled Water Droplet Impacting Superhydrophobic Surfaces in the Presence of Cold Air Flow, *Appl. Sci.* 7 (2017) 130.
- [34] C. Hao, Y. Liu, X. Chen, J. Li, M. Zhang, Y. Zhao, Z. Wang, Bioinspired Interfacial Materials with Enhanced Drop Mobility: From Fundamentals to Multifunctional Applications, *Small*. 12 (2016) 1825–1839.
- [35] R. Rioboo, M. Marengo, C. Tropea, Time evolution of liquid drop impact onto solid, dry surfaces, *Exp. Fluids*. 33 (2002) 112–124.
- [36] N.D. Patil, R. Bhardwaj, A. Sharma, Droplet impact dynamics on micropillared hydrophobic surfaces, *Exp. Therm. Fluid Sci.* 74 (2016) 195–206.
- [37] S. Baek, W. Kim, S. Jeon, K. Yong, Dual dimensional nanostructures with highly durable non-wetting properties under dynamic and underwater conditions, *Nanoscale*. 9 (2017) 6665–6673.
- [38] L. Chen, Z. Xiao, P.C.H. Chan, Y.K. Lee, Z. Li, A comparative study of droplet impact dynamics on a dual-scaled superhydrophobic surface and lotus leaf, *Appl. Surf. Sci.* 257 (2011) 8857–8863.

- [39] R. Ramachandran, K. Sobolev, M. Nosonovsky, Dynamics of droplet impact on hydrophobic/icephobic concrete with the potential for superhydrophobicity, *Langmuir*. 31 (2015) 1437–1444.
- [40] C. Mundo, M. Sommerfeld, C. Tropea, Droplet-wall collisions: Experimental studies of the deformation and breakup process, *Int. J. Multiph. Flow*. 21 (1995) 151–173.
- [41] Y. Shen, X. Wu, J. Tao, C. Zhu, Y. Lai, Z. Chen, Icephobic materials: Fundamentals, performance evaluation, and applications, *Prog. Mater. Sci.* 103 (2019) 509–557.
- [42] L. Boinovich, A.M. Emelyanenko, V. V. Korolev, A.S. Pashinin, Effect of wettability on sessile drop freezing: When superhydrophobicity stimulates an extreme freezing delay, *Langmuir*. 30 (2014) 1659–1668.
- [43] P.G. Debenedetti, Supercooled and glassy water, *J. Phys. Condens. Matter*. 15 (2003) R1669–R1726.
- [44] N. Lin, X.Y. Liu, Correlation between hierarchical structure of crystal networks and macroscopic performance of mesoscopic soft materials and engineering principles, *Chem. Soc. Rev.* 44 (2015) 7881–7915.
- [45] D. Chen, M.D. Gelenter, M. Hong, R.E. Cohen, G.H. McKinley, Icephobic surfaces induced by interfacial nonfrozen water, *ACS Appl. Mater. Interfaces*. 9 (2017) 4202–4214.
- [46] S. Karthika, T.K. Radhakrishnan, P. Kalaichelvi, A Review of Classical and Nonclassical Nucleation Theories, *Cryst. Growth Des.* 16 (2016) 6663–6681.
- [47] M. Rahimi, A. Afshari, E. Thormann, Effect of Aluminum Substrate Surface Modification on Wettability and Freezing Delay of Water Droplet at Subzero Temperatures, *ACS Appl. Mater. Interfaces*. 8 (2016) 11147–11153.
- [48] Z. Zhang, X.Y. Liu, Control of ice nucleation: Freezing and antifreeze strategies, *Chem. Soc. Rev.* 47 (2018) 7116–7139.
- [49] H.R. Pruppacher, J.D. Klett, *Microphysics of Clouds and Precipitation*, 2nd ed., Springer Netherlands, New York, Boston, Dordrecht, London, Moscow, 2010.
- [50] M.K. Politovich, Aviation Meteorology: Aircraft Icing, in: *Encycl. Atmos. Sci.*, Elsevier, 2015: pp. 160–165.
- [51] H. Sojoudi, M. Wang, N.D. Boscher, G.H. McKinley, K.K. Gleason, Durable and scalable icephobic surfaces: Similarities and distinctions from superhydrophobic surfaces, *Soft Matter*. 12 (2016) 1938–1963.
- [52] J. Zou, L. Ye, J. Ge, C. Zhao, Novel fiber optic sensor for ice type detection, *Meas. J. Int. Meas. Confed.* 46 (2013) 881–886.
- [53] P. Kim, T.S. Wong, J. Alvarenga, M.J. Kreder, W.E. Adorno-Martinez, J. Aizenberg, Liquid-infused nanostructured surfaces with extreme anti-ice and anti-frost performance, *ACS Nano*. 6 (2012) 6569–6577.
- [54] T. Young, III. An essay on the cohesion of fluids, *Philos. Trans. R. Soc. London*. 95 (1805) 65–87.
- [55] A.J. Meuler, J.D. Smith, K.K. Varanasi, J.M. Mabry, G.H. McKinley, R.E. Cohen, Relationships between water wettability and ice adhesion, *ACS Appl. Mater. Interfaces*. 2 (2010) 3100–3110.
- [56] L. Gao, T.J. McCarthy, Teflon is Hydrophilic. Comments on Definitions of Hydrophobic, Shear versus Tensile Hydrophobicity, and Wettability Characterization, *Langmuir*. 24 (2008) 9183–9188.
- [57] I.A. Ryzhkin, V.F. Petrenko, Physical Mechanisms Responsible for Ice Adhesion, *J. Phys. Chem. B*. 101 (1997) 6267–6270.

- [58] A. Dotan, H. Dodiuk, C. Laforte, S. Kenig, The Relationship between Water Wetting and Ice Adhesion, *J. Adhes. Sci. Technol.* 23 (2009) 1907–1915.
- [59] F. Guerin, C. Laforte, M.I. Farinas, J. Perron, Analytical model based on experimental data of centrifuge ice adhesion tests with different substrates, *Cold Reg. Sci. Technol.* 121 (2016) 93–99.
- [60] D.L. Beemer, W. Wang, A.K. Kota, Durable gels with ultra-low adhesion to ice, *J. Mater. Chem. A* 4 (2016) 18253–18258.
- [61] J. Chen, J. Liu, M. He, K. Li, D. Cui, Q. Zhang, X. Zeng, Y. Zhang, J. Wang, Y. Song, Superhydrophobic surfaces cannot reduce ice adhesion, *Appl. Phys. Lett.* 101 (2012) 18–21.
- [62] F. Wang, F. Lv, Y. Liu, C. Li, Y. Lv, Ice adhesion on different microstructure superhydrophobic aluminum surfaces, *J. Adhes. Sci. Technol.* 27 (2013) 58–67.
- [63] P. Guo, Y. Zheng, M. Wen, C. Song, Y. Lin, L. Jiang, Icephobic/anti-icing properties of micro/nanostructured surfaces, *Adv. Mater.* 24 (2012) 2642–2648.
- [64] S.A. Kulinich, M. Farzaneh, Ice adhesion on super-hydrophobic surfaces, *Appl. Surf. Sci.* 255 (2009) 8153–8157.
- [65] M. Susoff, K. Siegmund, C. Pfaffenroth, M. Hirayama, Evaluation of icephobic coatings - Screening of different coatings and influence of roughness, *Appl. Surf. Sci.* 282 (2013) 870–879.
- [66] W. Cui, Y. Jiang, K. Mielonen, T.A. Pakkanen, The verification of icephobic performance on biomimetic superhydrophobic surfaces and the effect of wettability and surface energy, *Appl. Surf. Sci.* 466 (2019) 503–514.
- [67] S. Ozbay, H.Y. Erbil, Ice accretion by spraying supercooled droplets is not dependent on wettability and surface free energy of substrates, *Colloids Surfaces A Physicochem. Eng. Asp.* 504 (2016) 210–218.
- [68] S.A. Kulinich, M. Farzaneh, How Wetting Hysteresis Influences Ice Adhesion Strength on Superhydrophobic Surfaces, *Langmuir*. 25 (2009) 8854–8856.
- [69] N. Vogel, R.A. Belisle, B. Hatton, T.S. Wong, J. Aizenberg, Transparency and damage tolerance of patternable omniphobic lubricated surfaces based on inverse colloidal monolayers, *Nat. Commun.* 4 (2013) 1–10.
- [70] Q. Liu, Y. Yang, M. Huang, Y. Zhou, Y. Liu, X. Liang, Durability of a lubricant-infused Electro spray Silicon Rubber surface as an anti-icing coating, *Appl. Surf. Sci.* 346 (2015) 68–76.
- [71] S. Wang, K. Liu, X. Yao, L. Jiang, Bioinspired Surfaces with Superwettability: New Insight on Theory, Design, and Applications, *Chem. Rev.* 115 (2015) 8230–8293.
- [72] X. Zhang, F. Shi, J. Niu, Y. Jiang, Z. Wang, Superhydrophobic surfaces: From structural control to functional application, *J. Mater. Chem.* 18 (2008) 621–633.
- [73] R.A. Lawson, A.P.G. Robinson, Overview of materials and processes for lithography, in: *Front. Nanosci.*, Elsevier, 2016: pp. 1–90.
- [74] H. Samadian, H. Mobasheri, S. Hasanpour, R.F. Majidi, Electrospinning of Polyacrylonitrile Nanofibers and Simulation of Electric Field via Finite Element method, *Nanomedicine Res. J.* 2 (2017) 87–92.
- [75] M. Takeuchi, K. Sakamoto, K. Tsujimaru, M. Anpo, Photo-induced superhydrophilicity on TiO<sub>2</sub> thin films prepared by an ionized cluster beam deposition method, *Catal. Letters*. 131 (2009) 189–193.
- [76] Y. Zhuo, F. Wang, S. Xiao, J. He, Z. Zhang, One-Step Fabrication of Bioinspired Lubricant-Regenerable Icephobic Slippery Liquid-Infused Porous Surfaces, *ACS*

- Omega. 3 (2018) 10139–10144.
- [77] R. Gupta, A. Kumar, Bioactive materials for biomedical applications using sol-gel technology, *Biomed. Mater.* 3 (2008).
- [78] H. Zhang, H. Ding, M. Wei, C. Li, B. Wei, J. Zhang, Thin film encapsulation for organic light-emitting diodes using inorganic/organic hybrid layers by atomic layer deposition, *Nanoscale Res. Lett.* 10 (2015) 4–8.
- [79] M. Keeney, X.Y. Jiang, M. Yamane, M. Lee, S. Goodman, F. Yang, Nanocoating for biomolecule delivery using layer-by-layer self-assembly, *J. Mater. Chem. B.* 3 (2015) 8757–8770.
- [80] Q. Yang, Z. Lu, J. Liu, X. Lei, Z. Chang, L. Luo, X. Sun, Metal oxide and hydroxide nanoarrays: Hydrothermal synthesis and applications as supercapacitors and nanocatalysts, *Prog. Nat. Sci. Mater. Int.* 23 (2013) 351–366.
- [81] Y. Tian, B. Su, L. Jiang, Interfacial Material System Exhibiting Superwettability, *Adv. Mater.* 26 (2014) 6872–6897.
- [82] R. Förch, H. Schönherr, A.T.A. Jenkins, Appendix C: Contact Angle Goniometry, in: *Surf. Des. Appl. Biosci. Nanotechnol.*, Wiley-VCH Verlag GmbH & Co. KGaA, Weinheim, Germany, 2009: pp. 471–473.
- [83] T.H. Muster, C.A. Prestidge, Water adsorption kinetics and contact angles of pharmaceutical powders, *J. Pharm. Sci.* 94 (2005) 861–872.
- [84] L. Oberli, D. Caruso, C. Hall, M. Fabretto, P.J. Murphy, D. Evans, Condensation and freezing of droplets on superhydrophobic surfaces, *Adv. Colloid Interface Sci.* 210 (2014) 47–57.
- [85] Y. Zhao, Moving contact line problem: Advances and perspectives, in: *Theor. Appl. Mech. Lett.*, Elsevier, 2014: p. 34002.
- [86] R. Bhaskar, M. Ola, P.H. Patil, III. An essay on the cohesion of fluids, *Philos. Trans. R. Soc. London.* 95 (1805) 65–87.
- [87] R.N. Wenzel, Resistance of solid surfaces to wetting by water, *Ind. Eng. Chem.* 28 (1936) 988–994.
- [88] S. Han, R. Yang, C. Li, L. Yang, The Wettability and Numerical Model of Different Silicon Microstructural Surfaces, *Appl. Sci.* 9 (2019) 566.
- [89] A.B.D. Cassie, S. Baxter, Wettability of porous surfaces, *Trans. Faraday Soc.* 40 (1944) 546.
- [90] M. Kuang, J. Wang, L. Jiang, Bio-inspired photonic crystals with superwettability, *Chem. Soc. Rev.* 45 (2016) 6833–6854.
- [91] W. Barthlott, C. Neinhuis, Purity of the sacred lotus, or escape from contamination in biological surfaces, *Planta.* 202 (1997) 1–8.
- [92] L.B. Boinovich, A.M. Emelyanenko, Anti-icing Potential of Superhydrophobic Coatings, *Mendeleev Commun.* 23 (2013) 3–10.
- [93] A.V. Ruban, H.L. Skriver, J.K. Nørskov, Local equilibrium properties of metallic surface alloys, in: *Chem. Phys. Solid Surfaces*, 2002: pp. 1–29.
- [94] D.M. Mattox, Substrate (“Real”) Surfaces and Surface Modification, in: *Handb. Phys. Vap. Depos. Process.*, Elsevier, 2010: pp. 25–72.
- [95] J.M. Schuster, C.E. Schvezov, M.R. Rosenberger, Analysis of the Results of Surface Free Energy Measurement of Ti6Al4V by Different Methods, *Procedia Mater. Sci.* 8 (2015) 732–741.
- [96] D.E. Packham, Surface energy, surface topography and adhesion, *Int. J. Adhes. Adhes.* 23 (2003) 437–448.

- [97] W.A. Zisman, Influence of constitution on adhesion, *Ind. Eng. Chem.* 55 (1963) 18–38.
- [98] M. Gindl, G. Sinn, W. Gindl, A. Reiterer, S. Tschegg, A comparison of different methods to calculate the surface free energy of wood using contact angle measurements, *Colloids Surfaces A Physicochem. Eng. Asp.* 181 (2001) 279–287.
- [99] S. Wu, Calculation of interfacial tension in polymer systems, *J. Polym. Sci. Part C Polym. Symp.* 34 (1971) 19–30.
- [100] S. Wu, Polar and nonpolar interactions in adhesion, *J. Adhes.* 5 (1973) 39–55.
- [101] T. Nishino, M. Meguro, K. Nakamae, M. Matsushita, Y. Ueda, The Lowest Surface Free Energy Based on -CF<sub>3</sub> Alignment, *Langmuir.* 15 (2002) 4321–4323.
- [102] K. Li, S. Xu, W. Shi, M. He, H. Li, S. Li, X. Zhou, J. Wang, Y. Song, Investigating the effects of solid surfaces on Ice nucleation, *Langmuir.* 28 (2012) 10749–10754.
- [103] C. Wang, T. Fuller, W. Zhang, K.J. Wynne, Thickness dependence of ice removal stress for a polydimethylsiloxane nanocomposite: Sylgard 184, *Langmuir.* 30 (2014) 12819–12826.
- [104] T. Bharathidasan, S.V. Kumar, M.S. Bobji, R.P.S. Chakradhar, B.J. Basu, Effect of wettability and surface roughness on ice-adhesion strength of hydrophilic, hydrophobic and superhydrophobic surfaces, *Appl. Surf. Sci.* 314 (2014) 241–250.
- [105] B. Liu, K. Zhang, C. Tao, Y. Zhao, X. Li, K. Zhu, X. Yuan, Strategies for anti-icing: low surface energy or liquid-infused?, *RSC Adv.* 6 (2016) 70251–70260.
- [106] R. Dou, J. Chen, Y. Zhang, X. Wang, D. Cui, Y. Song, L. Jiang, J. Wang, Anti-icing coating with an aqueous lubricating layer, *ACS Appl. Mater. Interfaces.* 6 (2014) 6998–7003.
- [107] K. Zhu, X. Li, J. Su, H. Li, Y. Zhao, X. Yuan, Improvement of anti-icing properties of low surface energy coatings by introducing phase-change microcapsules, *Polym. Eng. Sci.* 58 (2018) 973–979.
- [108] J.G. Duman, Antifreeze and Ice Nucleator Proteins in Terrestrial Arthropods, *Annu. Rev. Physiol.* 63 (2001) 327–357.
- [109] X. Yin, Y. Zhang, D. Wang, Z. Liu, Y. Liu, X. Pei, B. Yu, F. Zhou, Integration of Self-Lubrication and Near-Infrared Photothermogenesis for Excellent Anti-Icing/Deicing Performance, *Adv. Funct. Mater.* 25 (2015) 4237–4245.
- [110] M. He, H. Li, J. Wang, Y. Song, Superhydrophobic surface at low surface temperature, *Appl. Phys. Lett.* 98 (2011).
- [111] L. Mishchenko, B. Hatton, V. Bahadur, J.A. Taylor, T. Krupenkin, J. Aizenberg, Design of ice-free nanostructured surfaces based on repulsion of impacting water droplets, *ACS Nano.* 4 (2010) 7699–7707.
- [112] K.K. Varanasi, T. Deng, J.D. Smith, M. Hsu, N. Bhate, Frost formation and ice adhesion on superhydrophobic surfaces, *Appl. Phys. Lett.* 97 (2010) 234102.
- [113] S.A. Kulinich, S. Farhadi, K. Nose, X.W. Du, Superhydrophobic surfaces: Are they really ice-repellent?, *Langmuir.* 27 (2011) 25–29.
- [114] Z. Guo, F. Yang, Biomimetic Superhydrophobic Materials Applied for Anti-icing/Frosting, in: Z.G. and F. Yang (Ed.), *Surfaces Interfaces Biomim. Superhydrophobic Mater.*, First, Wiley-VCH Verlag GmbH & Co. KGaA, Weinheim, Germany, 2018: pp. 273–371.
- [115] T.S. Wong, S.H. Kang, S.K.Y. Tang, E.J. Smythe, B.D. Hatton, A. Grinthal, J. Aizenberg, Bioinspired self-repairing slippery surfaces with pressure-stable omniphobicity, *Nature.* 477 (2011) 443–447.
- [116] M. Nosonovsky, Slippery when wetted, *Nature.* 477 (2011) 412–413.

- [117] C. Howell, A. Grinthal, S. Sunny, M. Aizenberg, J. Aizenberg, Designing Liquid-Infused Surfaces for Medical Applications: A Review, *Adv. Mater.* 30 (2018) 1–26.
- [118] H. Niemelä-Anttonen, H. Koivuluoto, M. Tuominen, H. Teisala, P. Juuti, J. Haapanen, J. Harra, C. Stenroos, J. Lahti, J. Kuusipalo, J.M. Mäkelä, P. Vuoristo, Icephobicity of Slippery Liquid Infused Porous Surfaces under Multiple Freeze–Thaw and Ice Accretion–Detachment Cycles, *Adv. Mater. Interfaces.* 5 (2018) 1–8.
- [119] H. Bazyar, S. Javadpour, R.G.H. Lammertink, On the Gating Mechanism of Slippery Liquid Infused Porous Membranes, *Adv. Mater. Interfaces.* 3 (2016) 1600025.
- [120] K. Manabe, K.H. Kyung, S. Shiratori, Biocompatible slippery fluid-infused films composed of chitosan and alginate via layer-by-layer self-assembly and their antithrombogenicity, *ACS Appl. Mater. Interfaces.* 7 (2015) 4763–4771.
- [121] Z. Wang, Z. Guo, Biomimetic self-slippery and transferable transparent lubricant-infused functional surfaces, *Nanoscale.* 10 (2018) 19879–19889.
- [122] W. He, P. Liu, J. Zhang, X. Yao, Emerging Applications of Bioinspired Slippery Surfaces in Biomedical Fields, *Chem. - A Eur. J.* 24 (2018) 14864–14877.
- [123] J. Li, E. Ueda, D. Paulssen, P.A. Levkin, Slippery Lubricant-Infused Surfaces: Properties and Emerging Applications, *Adv. Funct. Mater.* 29 (2019) 1–13.
- [124] P. Irajizad, M. Hasnain, N. Farokhnia, S.M. Sajadi, H. Ghasemi, Magnetic slippery extreme icephobic surfaces, *Nat. Commun.* 7 (2016) 1–7.
- [125] I. Oh, C. Keplinger, J. Cui, J. Chen, G.M. Whitesides, J. Aizenberg, Y. Hu, Dynamically Actuated Liquid-Infused Poroelastic Film with Precise Control over Droplet Dynamics, *Adv. Funct. Mater.* 28 (2018) 1–9.
- [126] M. Tenjimbayashi, S. Nishioka, Y. Kobayashi, K. Kawase, J. Li, J. Abe, S. Shiratori, A Lubricant-Sandwiched Coating with Long-Term Stable Anticorrosion Performance, *Langmuir.* 34 (2018) 1386–1393.
- [127] Y. Zhuo, V. Håkonsen, Z. He, S. Xiao, J. He, Z. Zhang, Enhancing the Mechanical Durability of Icephobic Surfaces by Introducing Autonomous Self-Healing Function, *ACS Appl. Mater. Interfaces.* 10 (2018) 11972–11978.
- [128] J.D. Smith, R. Dhiman, S. Anand, E. Reza-Garduno, R.E. Cohen, G.H. McKinley, K.K. Varanasi, Droplet mobility on lubricant-impregnated surfaces, *Soft Matter.* 9 (2013) 1772–1780.
- [129] S. Sett, X. Yan, G. Barac, L.W. Bolton, N. Miljkovic, Lubricant-Infused Surfaces for Low-Surface-Tension Fluids: Promise versus Reality, *ACS Appl. Mater. Interfaces.* 9 (2017) 36400–36408.
- [130] X. Sun, V.G. Damle, S. Liu, K. Rykaczewski, Bioinspired Stimuli-Responsive and Antifreeze-Secreting Anti-Icing Coatings, *Adv. Mater. Interfaces.* 2 (2015) 25–27.
- [131] Q. Fu, X. Wu, D. Kumar, J.W.C. Ho, P.D. Kanhere, N. Srikanth, E. Liu, P. Wilson, Z. Chen, Development of sol-gel icephobic coatings: Effect of surface roughness and surface energy, *ACS Appl. Mater. Interfaces.* 6 (2014) 20685–20692.
- [132] Y. Wang, J. Liu, M. Li, Q. Wang, Q. Chen, The icephobicity comparison of polysiloxane modified hydrophobic and superhydrophobic surfaces under condensing environments, *Appl. Surf. Sci.* 385 (2016) 472–480.
- [133] E.J.Y. Ling, V. Uong, J.S. Renault-Crispo, A.M. Kietzig, P. Servio, Reducing Ice Adhesion on Nonsmooth Metallic Surfaces: Wettability and Topography Effects, *ACS Appl. Mater. Interfaces.* 8 (2016) 8789–8800.
- [134] A. Fernández, A. Francone, L.H. Thamdrup, A. Johansson, B. Bilenberg, T. Nielsen, M. Guttman, C.M. Sotomayor Torres, N. Kehagias, Design of Hierarchical Surfaces for

- Tuning Wetting Characteristics, *ACS Appl. Mater. Interfaces*. 9 (2017) 7701–7709.
- [135] N. Hidayah, M. Mustapha, H. Ismail, M. Kamarol, Linear low-density polyethylene/silicone rubber nanocomposites, *J. Elastomers Plast.* 50 (2018) 36–57.
- [136] T. Moriya, K. Manabe, M. Tenjimbayashi, K. Suwabe, H. Tsuchiya, T. Matsubayashi, W. Navarrini, S. Shiratori, A superrepellent coating with dynamic fluorine chains for frosting suppression: effects of polarity, coalescence and ice nucleation free energy barrier, *RSC Adv.* 6 (2016) 92197–92205.
- [137] P.W. Wilson, W. Lu, H. Xu, P. Kim, M.J. Kreder, J. Alvarenga, J. Aizenberg, Inhibition of ice nucleation by slippery liquid-infused porous surfaces (SLIPS), *Phys. Chem. Chem. Phys.* 15 (2013) 581–585.
- [138] R. Ramachandran, M. Kozhukhova, K. Sobolev, M. Nosonovsky, Anti-Icing Superhydrophobic Surfaces: Controlling Entropic Molecular Interactions to Design Novel Icephobic Concrete, *Entropy*. 18 (2016) 132.
- [139] M.J. Coady, M. Wood, G.Q. Wallace, K.E. Nielsen, A.M. Kietzig, F. Laguñé-Labarthet, P.J. Ragogna, Icephobic Behavior of UV-Cured Polymer Networks Incorporated into Slippery Lubricant-Infused Porous Surfaces: Improving SLIPS Durability, *ACS Appl. Mater. Interfaces*. 10 (2018) 2890–2896.
- [140] I. Okada, S. Shiratori, High-transparency, self-standable Gel-SLIPS fabricated by a facile nanoscale phase separation, *ACS Appl. Mater. Interfaces*. 6 (2014) 1502–1508.
- [141] X. He, W. Qiang, C. Du, Q. Shao, X. Zhang, Y. Deng, Modification of lubricant infused porous surface for low-voltage reversible electrowetting, *J. Mater. Chem. A*. 5 (2017) 19159–19167.
- [142] M.I. Jamil, A. Ali, F. Haq, Q. Zhang, X. Zhan, F. Chen, Icephobic Strategies and Materials with Superwettability: Design Principles and Mechanism, *Langmuir*. 34 (2018) 15425–15444.
- [143] M. Tenjimbayashi, R. Togasawa, K. Manabe, T. Matsubayashi, T. Moriya, M. Komine, S. Shiratori, Liquid-Infused Smooth Coating with Transparency, Super-Durability, and Extraordinary Hydrophobicity, *Adv. Funct. Mater.* 26 (2016) 6693–6702.
- [144] P. Zhang, H. Chen, L. Zhang, D. Zhang, Anti-adhesion effects of liquid-infused textured surfaces on high-temperature stainless steel for soft tissue, *Appl. Surf. Sci.* 385 (2016) 249–256.
- [145] C. Zhang, Y. Xia, H. Zhang, N.S. Zacharia, Surface Functionalization for a Nontextured Liquid-Infused Surface with Enhanced Lifetime, *ACS Appl. Mater. Interfaces*. 10 (2018) 5892–5901.
- [146] K. Rykaczewski, S. Anand, S.B. Subramanyam, K.K. Varanasi, Mechanism of frost formation on lubricant-impregnated surfaces, *Langmuir*. 29 (2013) 5230–5238.
- [147] P. Zhang, H. Chen, L. Zhang, T. Ran, D. Zhang, Transparent self-cleaning lubricant-infused surfaces made with large-area breath figure patterns, *Appl. Surf. Sci.* 355 (2015) 1083–1090.
- [148] M.J. Nine, T.T. Tung, F. Alotaibi, D.N.H. Tran, D. Losic, Facile Adhesion-Tuning of Superhydrophobic Surfaces between “Lotus” and “Petal” Effect and Their Influence on Icing and Deicing Properties, *ACS Appl. Mater. Interfaces*. 9 (2017) 8393–8402.
- [149] J. Zhang, L. Wu, B. Li, L. Li, S. Seeger, A. Wang, Evaporation-induced transition from nepenthes pitcher-inspired slippery surfaces to lotus leaf-inspired superoleophobic surfaces, *Langmuir*. 30 (2014) 14292–14299.
- [150] M. Tenjimbayashi, J.Y. Park, J. Muto, Y. Kobayashi, R. Yoshikawa, Y. Monnai, S. Shiratori, In Situ Formation of Slippery-Liquid-Infused Nanofibrous Surface for a

- Transparent Antifouling Endoscope Lens, *ACS Biomater. Sci. Eng.* 4 (2018) 1871–1879.
- [151] P. Kim, T.S. Wong, J. Alvarenga, M.J. Kreder, W.E. Adorno-Martinez, J. Aizenberg, Liquid-infused nanostructured surfaces with extreme anti-ice and anti-frost performance, *ACS Nano*. 6 (2012) 6569–6577.





## WENJUAN CUI

---

*The accumulation of ice on exposed outdoor infrastructures can cause serious economic losses and catastrophic events.*

*The thesis focuses on the verification of the icephobic performance of bio-inspired superhydrophobic surfaces and lubricant-infused slippery surfaces. The effects of their surface properties on icephobic performance have been investigated. Typical industrial application areas are in the prevention of ice formation on aerospace vehicles, windmill blades, and ground transportation.*



UNIVERSITY OF  
EASTERN FINLAND

*uef.fi*

**PUBLICATIONS OF  
THE UNIVERSITY OF EASTERN FINLAND**  
*Dissertations in Forestry and Natural Sciences*

ISBN 978-952-61-3238-9  
ISSN 1798-5668